Prediction of Reoxidation Inclusion Composition in Casting of Steel

LIANG WANG and CHRISTOPH BECKERMANN

A model is developed to calculate the composition of reoxidation inclusions that form during pouring of steel castings. The software package Thermo-Calc is used to obtain the inclusion phase fractions and compositions as a function of the temperature and oxygen content of the steel. Oxygen is assumed to be continually absorbed by the steel until the liquidus temperature is reached. Both lever rule and Scheil-type analyses are performed. The model is applied to reoxidation of two carbon steels, one low-alloy steel and one high-alloy steel. The effects of variations in the steel composition and the oxygen absorption rate on the inclusion composition are investigated in a parametric study. The mass fraction of absorbed oxygen is determined by matching predicted with previously measured reoxidation inclusion compositions for the various steels. Good agreement is obtained for most phases present in the inclusions. Interestingly, the agreement in the inclusion compositions occurs for all steel grades when the percentage of absorbed oxygen is equal to 0.9 wt pct. This value is explained using a separate model for the rate of oxygen absorption at the steel-atmosphere interface. Various scenarios are outlined that allow for the 0.9 wt pct of absorbed oxygen to be achieved. The model is then used to calculate the amount of alloy elements consumed and inclusions formed as a function of the oxygen boundary layer thickness in the atmosphere and the integrated free surface area of the liquid steel during pouring. It is found that for unprotected liquid steel transfer operations, such as tapping and ladle filling, the integrated free surface area and exposure time product can reach values of the order of 100 m^2 s per ton of steel, and that the air-to-steel volume ratio during pouring can be as large as 40. It is concluded that, in order to create a comprehensive tool for simulating reoxidation formation, more detailed models are needed for the external oxygen transfer in the atmosphere, the flow of the liquid steel during pouring, and the internal transport and reactions of chemical species in the steel.

I. INTRODUCTION

INCLUSIONS are a major cost factor in the production of steel castings. Removing inclusions and refilling the defect areas with the weld metal account for approximately 20 pct of the direct cost of steel castings.[1] Reoxidation inclusions are the most common form of inclusions that are found in steel castings. Based on a survey of steel foundries, they account for approximately 83 pct of the inclusions in carbon and low-alloy steel castings and approximately 48 pct of the inclusions in high-alloy and stainless steel castings.[2] Reoxidation is defined as the reaction of elements in steel with oxygen during pouring of the (deoxidized) steel from the ladle into the mold. Oxygen may come from the surrounding atmosphere, refractories, slag, or the sand mold.[3] The atmosphere is generally believed to be the primary source of oxygen, and limiting the exposure of the steel to the atmosphere is an important consideration in designing pouring systems.

Large reoxidation inclusions often accumulate on the cope surface of steel castings, where they may be visible to the naked eye. They have a detrimental effect on machining and mechanical performance of steel castings and may cause casting rejection. An image of a typical reoxidation macroinclusion cut from a low-alloy steel casting is shown in Figure 1.[2] The inclusion has a diameter of about 2 mm and consists of 34 wt pct Al_2O_3, 46 wt pct SiO_2, and 20 wt pct MnO. Its globular shape indicates that a relatively large fraction of the oxide mixture was in liquid form during formation of the inclusion. Inside the inclusion, smaller particles that were presumably solid during formation are visible as well.

The objective of the current study is to predict the composition of reoxidation inclusions in the casting of steels in sand molds. This study is part of a larger project to model the entire process of reoxidation inclusion formation and transport in steel casting.[4] It is shown that the inclusion composition is very sensitive to the steel composition and the amount of oxygen absorbed at the steel-atmosphere interface. Available thermochemical analysis software is used, which enables parametric studies to be conducted that would be difficult to perform experimentally.

Reoxidation of liquid steel has been investigated extensively in the past.[5–14] All of these studies conclude that the oxidation rate is primarily controlled by the rate of oxygen transfer through the atmosphere to the surface of the steel. Only for very low alloy element concentrations, or in the presence of stable oxide films, do internal diffusion processes become important.[6,7,9–11] The fact that the oxidation rate is limited by atmospheric transport of oxygen is established in the above references by performing experiments where the O_2 gas partial pressure in the atmosphere is varied. The experiments show that the consumption of oxidizing elements is linearly proportional to the O_2 partial pressure. Only a few studies combine experiments with thermochemical modeling to predict oxidation of liquid

LIANG WANG, Graduate Research Assistant, and CHRISTOPH BECKERMANN, Professor, are with the Department of Mechanical and Industrial Engineering, The University of Iowa, Iowa City, IA 52242. Contact e-mail: becker@engineering.uiowa.edu

Manuscript submitted September 20, 2005.

iron-base alloys (*e.g.,* References 9 and 10). The use of thermochemical analysis software in modeling oxide inclusion formation has become possible only within the past decade. For example, Hsieh *et al.*[15] analyzed inclusion formation in low-alloy steel welds as a function of the weld metal composition using Thermo-Calc.[16] Similarly, Eijk *et al.*[17] predicted the evolution of inclusion composition in Ti deoxidized steel. Neither of the latter two studies considered reoxidation, where oxygen is continually transferred to the liquid steel.

The composition and other characteristics of reoxidation inclusions in steel castings have been studied in several projects conducted under the auspices of the Steel Founders' Society of America (SFSA).[1] Lyman and Boulger[18] measured inclusion compositions in carbon steel castings as a function of the Al content and the Mn/Si ratio. Griffin and Bates[19,20] investigated reoxidation inclusions in both low-alloy and high-alloy steel castings. Extensive use is made of these data in the current study in order to validate the predictions. In addition, the matching of measured and predicted inclusion compositions allows for considerable insight into the inclusion formation processes in steel casting, including the absorption of oxygen.

The following section briefly reviews the modeling of oxygen absorption at the steel surface. Section III explains the method used to predict the inclusion composition in the presence of oxygen absorption. Section IV presents the results of the predictions and the comparisons with measurements for carbon, low-alloy, and high-alloy steels. These results are discussed in Section V. The dependence of the reoxidation rate on the free surface area and the exposure time is examined in Section VI. The conclusions of the current study are summarized in Section VII.

II. REVIW OF THE MODELING OF THE OXYGEN ABSORPTION RATE

Reoxidation of the liquid steel during pouring is assumed to be controlled by the transfer of O_2 gas from the atmosphere to the atmosphere-steel interface.[5–14] There, the oxygen reacts with the elements in the steel to form reoxidation inclusions. As illustrated in Figure 2, the oxygen absorption rate can be modeled as[11]

$$\frac{dn^{O}}{dt} = \frac{2\rho_a A_s}{M_a}\frac{D_a^{O_2}}{\delta_a^{O_2}}(\bar{C}_a^{O_2} - \bar{C}_{as}^{O_2}) \qquad [1]$$

where n^{O} is the number of moles of oxygen absorbed by the molten steel (mol), t is time (s), ρ_a is the density of the atmosphere (g/cm^3), A_s is the surface area of the molten steel (cm^2), M_a is the molecular weight of the atmosphere (g/mol), $D_a^{O_2}$ is the mass diffusivity of O_2 gas in the atmosphere (cm^2/s), $\delta_a^{O_2}$ is the thickness of the concentration boundary layer of O_2 gas in the atmosphere (cm), $\bar{C}_a^{O_2}$ is the mole fraction of O_2 gas in the atmosphere far from the atmosphere-steel interface (mol/mol), and $\bar{C}_{as}^{O_2}$ is the mole fraction of O_2 gas in the atmosphere at the atmosphere-steel interface (mol/mol). The factor of 2 in Eq. [1] stems from the fact that 1 mole of absorbed O_2 decomposes into two moles of O in the steel. The boundary layer thickness, $\delta_a^{O_2}$, accounts for the transport properties and flow conditions of the atmosphere (as subsequently discussed); for example, a larger relative velocity between the steel and the atmosphere would result in a smaller boundary layer thickness and, therefore, according to Eq. [1], a larger oxygen absorption rate. The ratio $D_a^{O_2}/\delta_a^{O_2}$ (cm/s) can also be interpreted as a convective mass transfer coefficient.

Equation [1] can be rewritten in terms of partial pressures, by employing the ideal gas law, as

$$\frac{dn^{O}}{dt} = 2A_s\frac{D_a^{O_2}}{\delta_a^{O_2}}\frac{(p_a^{O_2} - p_{as}^{O_2})}{RT} \qquad [2]$$

where $p_a^{O_2}$ is the partial pressure of O_2 gas in the atmosphere far from the atmosphere-steel interface (Pa), $p_{as}^{O_2}$ is the partial pressure of O_2 gas in the atmosphere at the atmosphere-steel interface (Pa), R is the universal gas constant [R = 8.314×10^6 Pa cm^3/(mol K)], and T is the absolute temperature (K). The partial pressure of O_2 gas in the atmosphere at the atmosphere-steel interface, $p_{as}^{O_2}$, is much lower than $p_a^{O_2}$[11] and can be safely neglected. Then, it can be seen that the oxygen absorption rate is linearly proportional to the

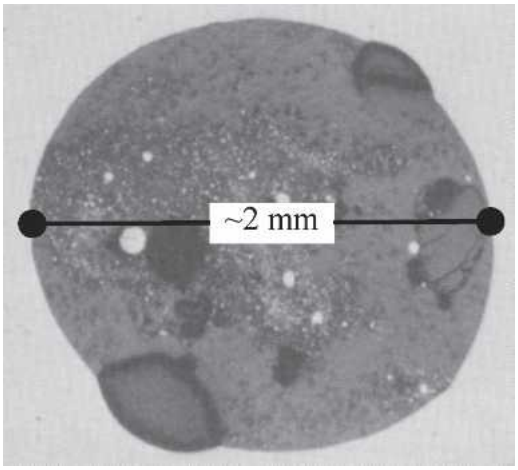

Fig. 1—Optical micrograph of a reoxidation inclusion cut from a steel casting; its bulk composition is 34 wt pct Al_2O_3, 46 wt pct SiO_2, and 20 wt pct MnO.[2]

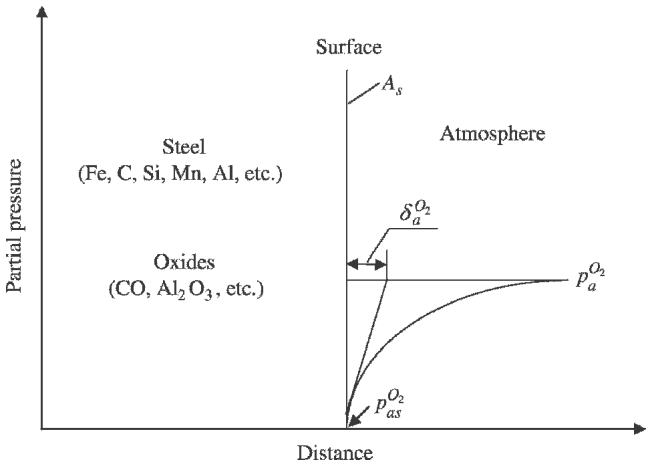

Fig. 2—Schematic illustration of oxygen absorption from the atmosphere and the oxygen boundary layer thickness during reoxidation of steel.

partial pressure of O_2 gas in the atmosphere, as mentioned in Section I.

For the purpose of the current study, it is necessary to convert the number of moles of absorbed oxygen into an oxygen mass fraction (per mass of steel). For a small oxygen mass relative to the mass of steel, the mass fraction, or simply "concentration," of absorbed oxygen, C^{O} (g/g), is given by

$$C^{o} = \frac{n^{o} M^{o}}{m_s} \qquad [3]$$

where M^{O} is the atomic weight of oxygen (g/mol). The mass of steel, m_s, is as of now undefined. However, for the preceding definition of a mass fraction to be useful, it must refer to that portion of the steel where the oxygen concentration is uniform. Obviously, the oxygen does not need to be evenly distributed in the steel during pouring, and m_s could be less than the total mass of steel poured. This issue is discussed further in Section V. After substitution of Eq. [3], Eq. [2] becomes[11]

$$\frac{dC^{o}}{dt} = \frac{2A_s M^{o}}{m_s} \frac{D_a^{o_2}}{\delta_a^{o_2}} \frac{p_a^{o_2}}{RT} \qquad [4]$$

In order to demonstrate the validity of Eq. [4] and to illustrate the effect of the boundary layer thickness, Eq. [4] is compared in the following to the experimental results of Sasai and Mizukami.[11] The experiments involved the oxidation of various iron melts that were either in a still state or stirred by an electromagnetic field. The melts were contained in crucibles and exposed at the top surface to various Ar-O_2 atmospheres at 1 atm. Both pure Fe melts and Fe-Al melts were investigated. For the Fe-Al melts, 0.1 wt pct aluminum was added to the electrolytic iron. In some experiments, 0.1 wt pct sulfur was added to the Fe and Fe-Al melts. For the experiments in the still state, 500 g of iron was melted in a cylindrical alumina crucible, having an inside diameter of 4 cm and a height of 15 cm. The partial pressure of O_2 gas in the Ar-O_2 atmosphere was varied over the range of 5 to 50 kPa. For the experiments in the stirred state, 70 to 80 kg of iron was melted in a cylindrical magnesia crucible, having an inside diameter of 22 cm and a height of 40 cm. Here, the partial pressure of O_2 gas was varied from 4 to 20 kPa. Other details of the experimental setup can be found in Reference 11. For the purpose of comparing the measured oxygen absorption rates to Eq. [4], the entire mass of the melt is used for m_s, implying that the oxygen is assumed to be well mixed inside the crucibles. The mass diffusivity of O_2 in Ar at 1600 °C is equal to 4.37 cm^2/s.[21]

Figure 3 shows the plots of the oxygen absorption rate as a function of the partial pressure of O_2 gas in the atmosphere. These plots are similar to Figures 7 and 8 in Reference 11. It can be seen from the log-log plots that the measured oxygen absorption rate (symbols) indeed varies linearly with the O_2 partial pressure, as predicted by Eq. [4]. This is true for the experimental data shown in Figure 3(a) for the still state and the data in Figure 3(b) for the stirred state. Not included in Figure 3(a) are the data from Reference 11 for aluminum-killed molten steel in the still state. For that case, Sasai and Mizukami[11] found a stable

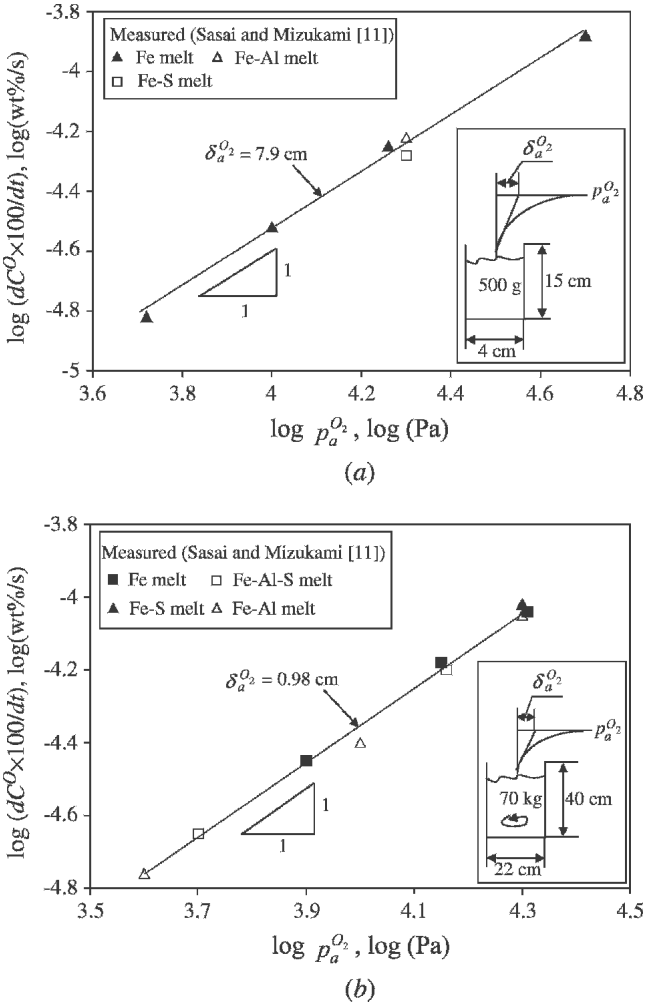

Fig. 3—Variation of the oxygen absorption rate in various Fe melts with the partial pressure of O_2 gas in the atmosphere: (*a*) still state and (*b*) stirred state.

oxide film to be present on the surface of the steel. Their analysis shows that the oxidation rate is then controlled by diffusion of oxygen in the oxide film. Stirring of the melt immediately broke up the oxide film, such that the oxidation rate was again controlled by transport of O_2 in the atmosphere. This indicates that stable oxide films that limit the oxidation rate are unlikely to be present during typical steel pouring operations, since the free surface flow during pouring is usually highly turbulent and unsteady. Figure 3 also shows that the measured oxygen absorption rates are not affected by the addition of Al or S to the iron melts; hence, neither internal diffusion processes or interfacial chemical reactions control the oxidation rate.[11]

In order to directly compare the predictions from Eq. [4] to the measured data, the boundary layer thickness, $\delta_a^{o_2}$, must be known. Unfortunately, it is difficult to estimate $\delta_a^{o_2}$ from the information provided in Reference 11. Therefore, $\delta_a^{o_2}$ was varied until the predictions fit the data (this corresponds to an up or down shift of the straight lines in Figure 3). Using this method, the boundary layer thickness was found to be equal to 7.9 cm for the experiments in the still state and 0.98 cm for the stirred state. As expected,

stirring the melt greatly decreases the boundary layer thickness in the atmosphere because of the increased relative velocity between the melt and the atmosphere. This decrease in $\delta_a^{O_2}$ causes an approximately eightfold increase in the oxygen absorption rate due to stirring. A detailed discussion regarding calculation of boundary layer thicknesses can be found in Section V. The values obtained previously for $\delta_a^{O_2}$ are realistic in that (1) even in the presence of strong stirring, $\delta_a^{O_2}$ is unlikely to be smaller than ~0.1 cm (Figure 19); and (ii) in the absence of stirring, $\delta_a^{O_2}$ can be expected to be of the same order of magnitude as the diameter of the crucible (4 cm) used in Reference 11.

III. CALCULATION OF REOXIDATION INCLUSION COMPOSITION

The composition of reoxidation inclusions as a function of steel composition and oxygen absorption rate is calculated in the current study using the software Thermo-Calc, Version P.[16] This widely used and carefully verified thermochemical analysis software for multiphase equilibrium calculations in multicomponent systems requires databases for the free energy functions and other basic data. The thermodynamic data for steel was taken from the TCAB steels/alloys database (TCFE) and that for the oxides from the SGTE substances database (SSUB). It is beyond the scope of the current study to provide an independent assessment of the accuracy of the Thermo-Calc predictions for the chemical systems being studied; however, the comparisons of measured and predicted inclusion compositions presented below may shed some light on its accuracy or potential shortcomings. Thermo-Calc is used in the current study in conjunction with an algorithm that steps down the temperature of the system and adds oxygen at a specified rate, as explained in the following discussion. This way, the cooling of the liquid steel and the absorption of oxygen from the atmosphere during pouring are approximated. Both full equilibrium (''lever rule'') and Scheil-type analyses are performed.

For a given temperature, T, pressure, P, and mass fraction of element i in the system, C^i, Thermo-Calc calculates, among other quantities, the mass fraction of each phase k in the system, f_k, and the mass fraction of each element i in phase k, C_k^i, assuming complete thermodynamic equilibrium. This relation between the input and output parameters can be written as

$$(T, P, C^i) \rightarrow (f_k^*, C_k^{i*}, \ldots) \qquad [5]$$

where the superscript ''*'' denotes an equilibrium value. Note that $C^i = \sum_k f_k^* C_k^{i*}$. The calculations are started at a temperature T_0 that corresponds to the pouring temperature of the steel (*e.g.,* 1600 °C). The initial values for C_i are given by the composition of the steel exiting from the ladle, and the pressure P is always kept at 1 atm. After completing the calculations at the temperature T_0 and outputting the phase fractions and compositions, the temperature is decreased by a small step, ΔT (less than 5 K), and the Thermo-Calc calculations represented by Eq. [5] are performed again at the new temperature. This procedure is repeated until room temperature (20 °C) is reached.

The absorption of oxygen is included in the Thermo-Calc calculations in the following manner. It is assumed that a certain total mass of oxygen per mass of steel, ΔC^O, is absorbed during the time interval between the initial temperature, T_0, and the liquidus temperature, T_l, of the steel. This total amount can be obtained by integrating the oxygen absorption rate given by Eq. [4] over the time interval the steel cools from T_0 to T_l. However, in Section IV, ΔC^O is simply treated as an adjustable parameter (also specified subsequently in units of weight percent instead of g/g). If there are n temperature steps between T_0 and T_l, the concentration of oxygen, C^O, is then increased at each step by an amount equal to $\Delta C^O/n$. Hence, as a first approximation, it is assumed that the oxygen absorption rate is constant during pouring. The initial oxygen concentration is assumed to be negligibly small, and no oxygen is added after the liquidus temperature is reached. Below the liquidus temperature, a solid shell forms that protects the steel from further fast oxidation.

The preceding procedure constitutes the complete algorithm for the so-called ''lever rule'' analysis. In the lever rule approach, diffusion is assumed to be infinitely fast, such that the chemical species are well mixed within each phase, and complete equilibrium is maintained at all times. As a consequence, previously formed phases can readily disappear at a lower temperature where they may not be thermodynamically stable. The assumption of infinitely fast diffusion can become particularly inappropriate once the steel solidifies, because the mass diffusivities of the various elements in steel are usually several orders of magnitude lower in the solid phase than in the liquid phase. Hence, as an alternative approach, a standard Scheil analysis is also performed. In the Scheil approach, diffusion in the solid is assumed to be negligibly small, while the liquid is still taken to be well mixed. Therefore, previously formed solid phases cannot dissolve. The calculation procedure for the Scheil analysis is similar to that for the lever rule method, except that at the beginning of each temperature step, the concentrations, C^i, are reset to the concentrations in the liquid steel, $C_l^{i'}$, from the previous temperature step (as denoted by the prime). Also, the new phase fractions are not simply the equilibrium values, f_k^*, but must be calculated from $f_k = f'_k + f_l^* \cdot f_k^*$. These and other procedures involved in the Scheil analysis are further explained in the Thermo-Calc manual.[16] The results presented in the next section illustrate the differences between the lever rule and Scheil approaches, as well as their effect on the prediction of reoxidation inclusion composition.

IV. RESULTS

The results of the reoxidation inclusion composition calculations are presented in this section separately for carbon steel and low- and high-alloy steels. The effects of the oxygen absorption rate, ΔC^O, and the steel composition are investigated, and the predicted inclusion compositions are compared with measured data.

A. *Carbon Steel*

The calculations for carbon steel are intended to correspond to the measurements of reoxidation inclusion

Table I. Nominal Compositions of the Steels Investigated in the Present Study (Weight Percent)

Steels	C	Si	Mn	S	P	Al	Cr	Ni	Mo
High-Al carbon steel	0.3	0.35	0.8	0.015	0.015	0.15	—	—	—
Low-Al carbon steel	0.3	0.35	0.4	0.015	0.015	0.05	—	—	—
Low-alloy steel	0.26	0.39	0.83	0.017	0.019	0.2	0.45	0.52	0.16
High-alloy steel, CF8M	0.05	1.33	1.0	0.03	0.03	—	19.5	10.5	2.5

composition by Lyman and Boulger.[18] In the experiments by Lyman and Boulger, approximately 400 carbon steel plate castings were poured from 62 experimental heats. The castings ranged in size from 41 to 113 kg (90 to 250 pounds). A green sand mold was used for most of the castings. The pouring temperature was taken as 1600 °C. Lyman and Boulger investigated both high-Al (0.15 wt pct) and low-Al (0.05 wt pct) carbon steels. The nominal steel compositions are provided in the first two rows of Table I. In some experiments, the Mn content was changed from the nominal values in Table I in order to investigate the effect of the Mn/Si ratio on inclusion composition; the Mn content was varied from 0.4 to 3.0 wt pct.

1. *High-Al carbon steel*

Figure 4 shows the evolution of the oxide mass percentages (per mass of steel) as a function of temperature for the high-Al carbon steel (Table I), calculated using the lever rule method. For the purpose of this figure, the mass fraction of absorbed oxygen, ΔC^{O}, is taken to be 0.9 wt pct (*i.e.,* 0.009 g/g). It can be seen that the total mass of all oxides increases almost linearly until the liquidus temperature, T_l, is reached (Figure 4(a)). The liquidus temperatures indicated in this and subsequent figures are those predicted by Thermo-Calc. The increase in the total oxide mass is not completely linear, even though the oxygen absorption rate is assumed to be constant, because of the different molecular weights of the various oxides that form. Below the liquidus temperature, the total oxide mass is approximately constant, since no more oxygen is added, except for small variations due to the continually changing composition of the oxides (Figure 4(b)).

Focusing first on the temperature range above liquidus (Figure 4(a)), it can be seen that the first oxide to form is solid alumina (Al_2O_3). After the entire Al is consumed, Si begins to oxidize (starting at approximately 1590 °C). At first, Si is oxidized in a reaction that consumes the alumina to form solid mullite ($3Al_2O_3\_2SiO_2$). After the alumina is completely converted, solid cristobalite (SiO_2) starts to form. At approximately the same temperature (~1585 °C), carbon monoxide gas (CO) also appears. Finally, at approximately 1560 °C, Mn begins to oxidize by forming liquid tephroite (Mn_2SiO_4), while the mullite and cristobalite mass percentages stay relatively constant. At the liquidus temperature, the oxide mixture consists of liquid tephroite (Mn_2SiO_4), solid mullite ($3Al_2O_3\_2SiO_2$), solid cristobalite (SiO_2), and CO gas; the exact percentages are listed in Table II. Obviously, the CO gas will occupy a very large volume and can be expected to escape from the liquid steel, but the present method treats the system as closed other than for the oxygen addition. The fact that more than half of the oxides (excluding CO gas) are in a liquid state agrees qualitatively

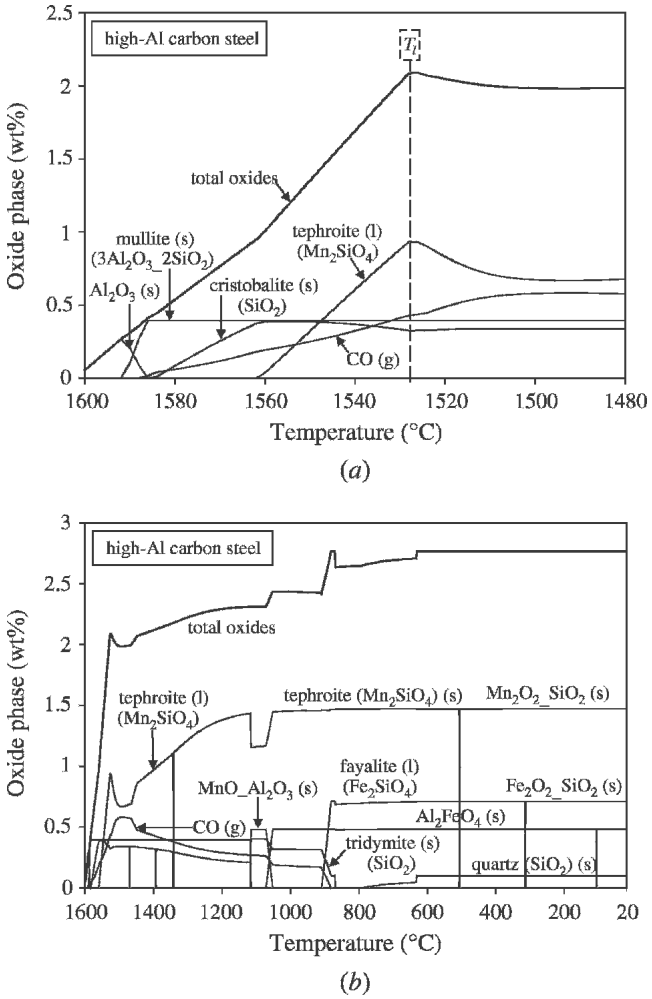

Fig. 4—Evolution of the mass percentage of the various oxide phases in high-Al carbon steel calculated using the lever rule method (ΔC^{O} = 0.9 wt pct). (*a*) Temperature range: 1600 °C to 1480 °C. (*b*) Temperature range: 1600 °C to 20 °C.

with the observation made in connection with Figure 1 regarding the globular shape of reoxidation inclusions.

For completeness, Figure 4(b) shows the predicted evolution of the oxide mass percentages all the way down to room temperature. The transformations below the liquidus temperature are unlikely to occur to completion in reality, because of the slow rate of mass diffusion in the solid and the fact that the CO gas will escape from the system. Therefore, the details of the transformations are not discussed here. Nonetheless, it is noteworthy that two iron containing oxides ($Fe_2O_2\_SiO_2$ and Al_2FeO_4) are predicted to be

Table II. Predicted and Equivalent Oxide Percentages for High-Al Carbon Steel

ΔC^O = 0.9 wt pct		Lever Rule Approach	Scheil Approach
Predicted oxide mass per mass of steel at the liquidus temperature (Wt pct); in parenthesis: percent of total	carbon monoxide (g) (CO)	0.429 (20.6 pct)	0.331 (20.1 pct)
	alumina (s) (Al_2O_3)	0 (0 pct)	0.254 (15.4 pct)
	cristobalite (s) (SiO_2)	0.325 (15.6 pct)	0.322 (19.6 pct)
	mullite (s) ($3Al_2O_3\_2SiO_2$)	0.395 (19.0 pct)	0 (0 pct)
	tephroite (l) (Mn_2SiO_4)	0.934 (44.8 pct)	0.738 (44.9 pct)
	total	2.083 (100 pct)	1.645 (100 pct)
Equivalent oxide percentage in inclusions, excluding CO gas (wt pct)	Al_2O_3	17.2	19.4
	SiO_2	43.1	41.2
	MnO	39.7	39.4
	total	100	100

thermodynamically stable at room temperature. As shown in Figure 4(a), no iron containing oxides are predicted to exist at the liquidus temperature (for ΔC^O = 0.9 wt pct). It is emphasized again that the results in Figure 4 are only the equilibrium oxide phase fractions as a function of temperature (and oxygen content), as predicted by Thermo-Calc using a lever rule analysis.

Figure 5 shows the corresponding results using the Scheil approach. As in Figure 4, the first oxide to form is solid alumina (Al_2O_3). However, once the entire Al is consumed (at about 1590 °C), the Al_2O_3 phase fraction remains constant, *i.e.,* the alumina is not consumed in other reactions. The inability of already formed oxides to be consumed in other reactions is the main consequence of the Scheil analysis, as noted in Section III. As a consequence, Si oxidizes (starting at 1590 °C) by directly forming cristobalite (SiO_2), instead of first consuming the alumina to form mullite. This constitutes the main difference to the lever rule predictions. The ensuing sequence of C and Mn oxidation is very similar to that observed in Figure 4. At the liquidus temperature, the oxide mixture is predicted by the Scheil analysis to consist of liquid tephroite (Mn_2SiO_4), solid cristobalite (SiO_2), solid alumina (Al_2O_3), and CO gas; again, the exact percentages are listed in Table II. No changes in the oxide phase percentages are predicted by the Scheil analysis for temperatures below liquidus. This illustrates a limitation of the Scheil analysis, since at least some further transformation of the liquid tephroite can be expected to occur at lower temperatures.

The oxide mass fractions predicted by the lever rule and Scheil methods at the liquidus temperature are compared in Table II. There is a difference of about 20 pct in the total mass of the oxides (per mass of steel) obtained by the two approaches. The individual oxide mass fractions are also different, but when viewed as a percent of the total mass of oxides formed (values in parenthesis in Table II), the similarities become apparent. The CO gas and liquid tephroite (Mn_2SiO_4) percentages for the lever rule and Scheil methods are nearly identical. Furthermore, by adding the mullite ($3Al_2O_3\_2SiO_2$) percentage (*i.e.,* 19 pct) to the two constituent oxide percentages, according to their molecular weights, the Al_2O_3 and SiO_2 percentages for the lever rule approach also become nearly identical to the ones for the Scheil analysis. The same comparison for the other steel grades investigated in the current study revealed similar agreement between the oxide percentages at the liquidus temperature (not shown here).

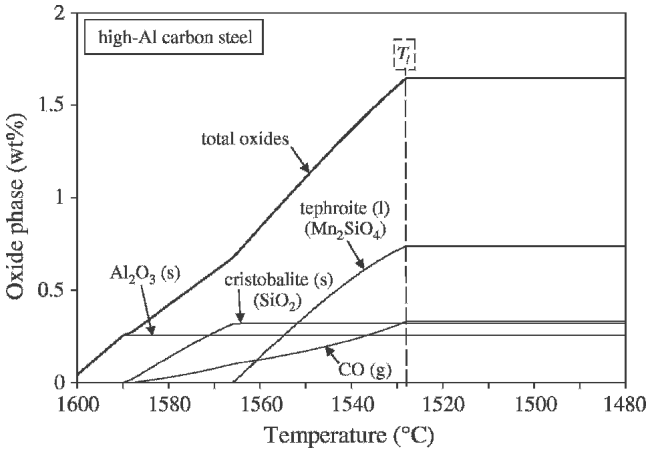

Fig. 5—Evolution of the mass percentage of the various oxide phases in high-Al carbon steel calculated using the Scheil method (ΔC^O = 0.9 wt pct).

As a next step, the predicted oxide percentages at the liquidus temperature are used to estimate the composition of the reoxidation inclusions, using the following conversion method. First, the mass fractions of the complex oxides (*e.g.,* Mn_2SiO_4 and $3Al_2O_3\_2SiO_2$) at the liquidus temperature are converted into equivalent mass fractions of simple oxides (*e.g.,* SiO_2, MnO, and Al_2O_3) using the chemical balances shown in Table III. It is such simple oxides that were measured in the experiments of Lyman and Boulger[18] and Griffin and Bates.[19,20] Then, the equivalent oxide mass fractions in the system (*i.e.,* per mass of steel) are converted to oxide mass fractions in the inclusion, where ''inclusion'' is defined as the sum of all oxides except the CO gas. The CO gas is excluded from the inclusion composition calculations, since it can be assumed to have escaped from the inclusion. The results of these conversions are shown in Table II for the Thermo-Calc predictions in Figures 4 and 5. It can be seen that the equivalent inclusion oxide percentages from the lever rule and Scheil analyses are very close to each other. Numerous additional calculations showed that the inclusion composition predictions from the lever rule and Scheil analyses are nearly identical for all steels investigated in the current study. Therefore, only results from the lever rule approach are presented in the remainder of this article. This was done for convenience only, because the lever rule computations are somewhat faster. Both the lever rule and the Scheil analyses have serious shortcomings or uncertainties, as

discussed above. Since the present ''conversion method'' yields the same inclusion composition for both approaches, a more complex model of the diffusion processes during inclusion formation does not appear to be warranted.

In Figures 4 and 5, the mass percentage of absorbed oxygen, ΔC^O, was taken to be 0.9 wt pct. The effect of the oxygen absorption rate on the oxide phase formation and the inclusion composition is investigated in Figure 6. Figure 6(a) shows that the total mass (per mass of steel) of all oxides increases almost linearly with the amount of oxygen absorbed. However, the percentages of the individual oxides at the liquidus temperature, as predicted by the lever rule method, vary considerably with ΔC^O. For $\Delta C^O <$ 0.4 wt pct, no CO gas and liquid tephroite are predicted to form, *i.e.,* all oxides are in a solid state. For larger oxygen absorption rates, the mass of liquid and gaseous oxides continually increases. For $\Delta C^O > 1.2$ wt pct, two Fe containing oxides form: solid Al_2FeO_4 and liquid fayalite (Fe_2SiO_4). According to the preceding discussion in connection with Figures 4 and 5 and Table II, similar results can be expected for the Scheil approach. The variation in the inclusion composition with ΔC^O, calculated using the above conversion method, is plotted in Figure 6(b). It can be seen that for very low oxygen absorption rates (*i.e.,* $\Delta C^O < 0.1$ wt pct), the inclusions are predicted to consist of Al_2O_3 only. With increasing ΔC^O, first SiO_2, then MnO, and finally FeO are predicted to be present in the inclusions. At the ΔC^O, where new oxides are formed, the percentages of the previously formed oxides decrease, since the inclusion oxide percentages must always total 100 pct.

Table III. Chemical Equations Used to Convert between Predicted and Equivalent Oxide Fractions

$3Al_2O_3\_2SiO_2 = 3Al_2O_3 + 2SiO_2$
$Mn_2SiO_4 = SiO_2 + 2MnO$
$Fe_2SiO_4 = SiO_2 + 2FeO$
$Al_2SiO_4 = SiO_2 + Al_2O_3$
$MnO\_Al_2O_3 = MnO + Al_2O_3$
$Cr_2FeO_4 = FeO + Cr_2O_3$

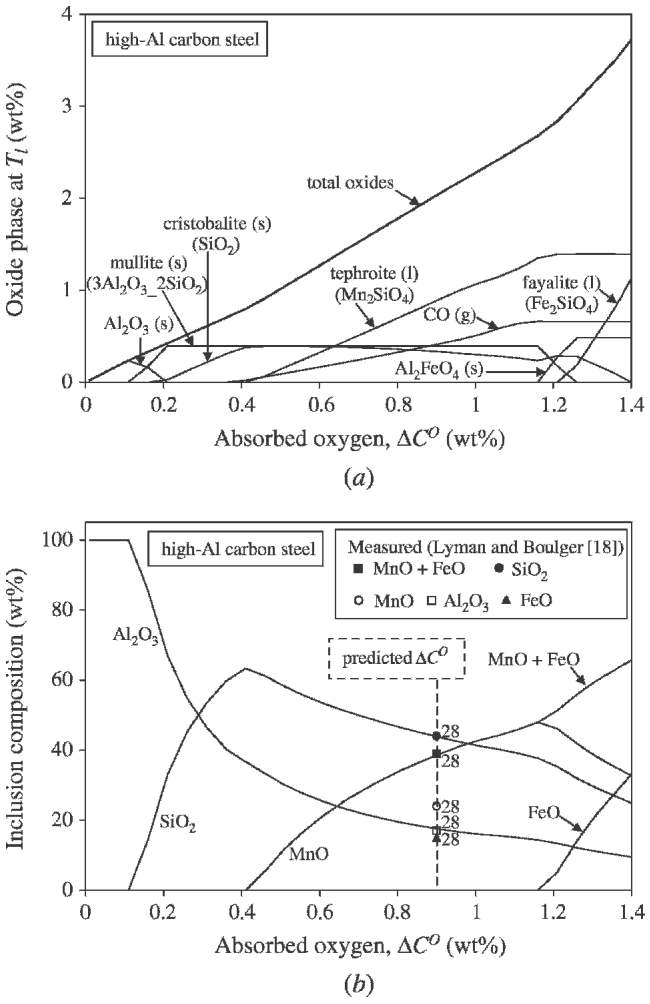

Fig. 6—Effect of the mass percentage of absorbed oxygen on the oxide mass percentages at the liquidus temperature and on the inclusion composition for high-Al carbon steel. (*a*) Mass percentage of oxide phases at the liquidus temperature (1528 °C, lever rule). (*b*) Inclusion composition (numbers next to symbols indicate number of samples).

The results in Figure 6(b) are now compared to the experimental measurements of Lyman and Boulger.[18] For the high-Al carbon steel castings with the nominal Mn content of 0.8 wt pct (Table I), the measured inclusion composition, averaged over 28 separate samples, is indicated as symbols in Figure 6(b). Unfortunately, measurement uncertainties were not reported by Lyman and Boulger,[18] and the spread in the measured compositions among the samples is not known. The symbols were shifted along the horizontal axis until the measured and predicted Al_2O_3 and SiO_2 contents agreed. As can be seen in Figure 6(b), an excellent match for both contents occurs for $\Delta C^O =$ 0.9 wt pct. For smaller ΔC^O, the Al_2O_3 and SiO_2 contents would be overpredicted, and the reverse would be true for larger ΔC^O. The MnO content is overpredicted and the calculated FeO percentage is zero for $\Delta C^O = 0.9$ wt pct; however, note that the sum of the measured MnO and FeO percentages agrees very well with the predicted MnO content at $\Delta C^O = 0.9$ wt pct. It is reasonable to add the MnO and FeO percentages because (1) once FeO forms it does so at the expense of MnO only (Figure 6(b)), and (2) FeO could form as the liquid tephroite (Mn_2SiO_4) is transformed during cooling to room temperature, as mentioned previously in connection with Figure 4(b). In summary, after adding the measured MnO and FeO percentages, all measured and predicted inclusion oxide percentages match for $\Delta C^O = 0.9$ wt pct. This agreement provides some confidence in the present method for calculating inclusion compositions, despite the uncertainty associated with the FeO content. The significance of the 0.9 wt pct value for the mass percentage of absorbed oxygen, ΔC^O, obtained by matching the measured and predicted inclusion compositions, is discussed in Section V.

Figures 7 through 10 explore the effect of variations in the steel composition on oxide formation and inclusion composition. In these figures, the mass percentage of absorbed oxygen is kept constant at $\Delta C^O = 0.9$ wt pct. In Figure 7, the Mn content is varied from 0.1 to 3.6 wt pct. The resulting effect on the oxide percentages at the liquidus temperature (predicted by the lever rule method) is shown in Figure 7(a). The total mass of all oxides (per mass of steel) increases, up to a Mn content of 2.3 wt pct, even though the amount of absorbed oxygen is constant. As

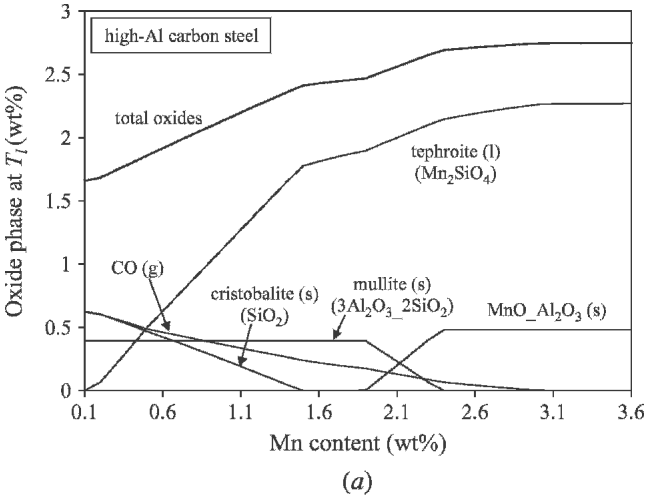

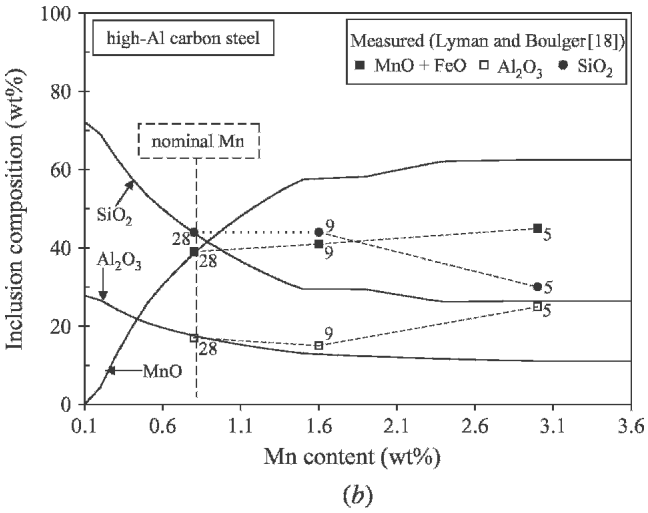

Fig. 7—Effect of the Mn content on the oxide mass percentages at the liquidus temperature and on the inclusion composition for high-Al carbon steel (ΔC^O = 0.9 wt pct). (*a*) Mass percentage of oxide phases at the liquidus temperature (1528 °C, lever rule). (*b*) Inclusion composition (numbers next to symbols indicate number of samples).

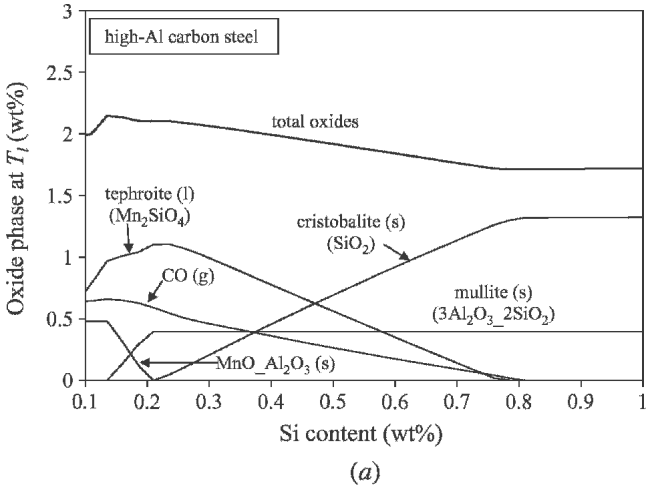

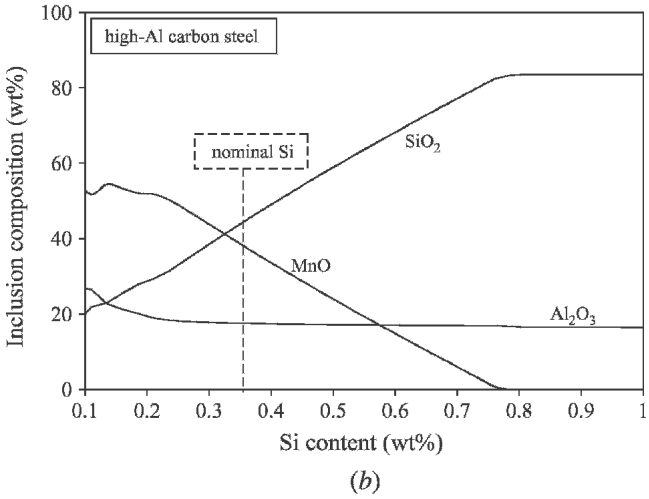

Fig. 8—Effect of the Si content on the oxide mass percentages at the liquidus temperature and on the inclusion composition for high-Al carbon steel (ΔC^O = 0.9 wt pct). (*a*) Mass percentage of oxide phases at the liquidus temperature (1528 °C, lever rule). (*b*) Inclusion composition.

expected, the percentage of Mn containing oxides, in particular liquid tephroite, increases with increasing Mn content. The percentage of CO gas decreases with increasing Mn content and no CO gas is formed for a Mn content above about 3.0 wt pct. The predicted inclusion composition is plotted as a function of the Mn content in Figure 7(b). For a Mn content in the steel of up to about 1.6 wt pct, the percentage of MnO in the inclusions increases strongly with increasing Mn content, while those of SiO_2 and Al_2O_3 decrease proportionally. Beyond 1.6 wt pct Mn, the inclusion composition is predicted to be approximately independent of the Mn content in the steel.

Also included in Figure 7(b) are the inclusion compositions measured by Lyman and Boulger[18] for Mn contents of 0.8 wt pct (nominal), 1.6 wt pct, and 3.0 wt pct (for the high-Al carbon steel of this subsection). As in Figure 6(b), the measured MnO and FeO contents are summed up. While the measured and predicted inclusion compositions agree well for the nominal Mn content of 0.8 wt pct, as already observed in Figure 6(b), some disagreement is present at the two higher Mn contents. The MnO content in the inclusion is predicted to increase more strongly with increasing Mn content in the steel than measured. Even though there is a relatively poor agreement at 1.6 wt pct Mn, the measured trend of the SiO_2 content in the inclusion decreasing for an increase in the Mn content from 0.8 to 3.0 wt pct is captured correctly by the calculations. The higher value of the measured Al_2O_3 percentage at 3.0 wt pct Mn, relative to the ones at the lower Mn contents, is difficult to explain since the Al content in the steel was presumably held constant and, from the predictions in Figure 7(b), the Al_2O_3 content is not expected to be a strong function of the Mn content in the range of interest. Note that, since the oxide inclusion percentages must add up to 100, a higher percentage in one oxide will necessarily cause other percentages to be smaller. Hence, this could explain the relative large disagreement between the measured and predicted MnO contents at 3.0 wt pct Mn. One possible explanation for the higher Al_2O_3 percentage measured at 3.0 wt pct Mn may be that more Al_2O_3 deoxidation particles are "captured" by the liquid tephroite, since the

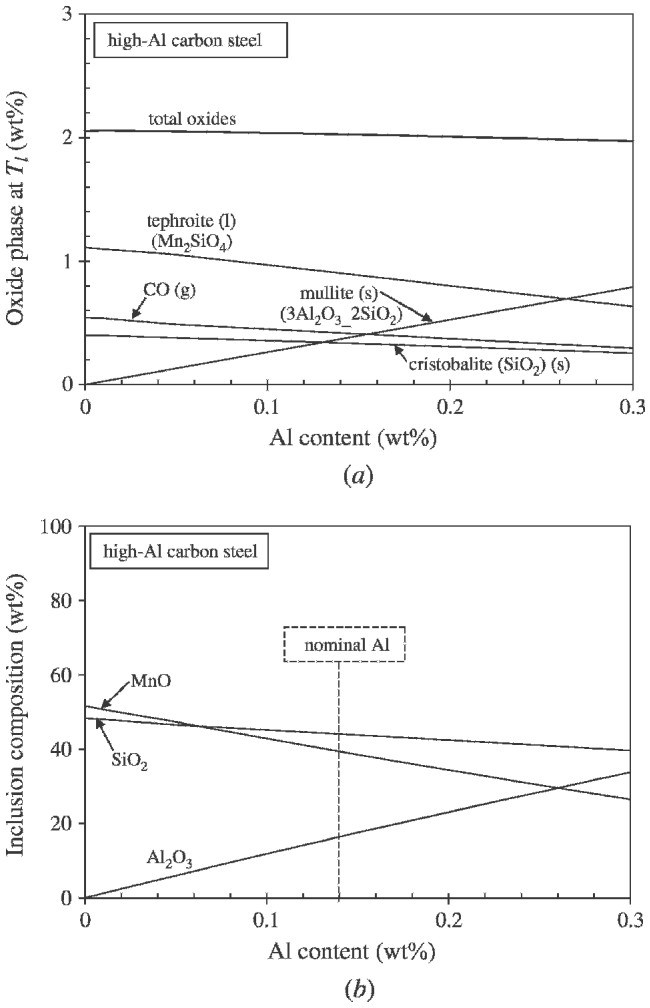

Fig. 9—Effect of the Al content on the oxide mass percentages at the liquidus temperature and on the inclusion composition for high-Al carbon steel (ΔC^O = 0.9 wt pct). (*a*) Mass percentage of oxide phases at the liquidus temperature (1528 °C, lever rule). (*b*) Inclusion composition.

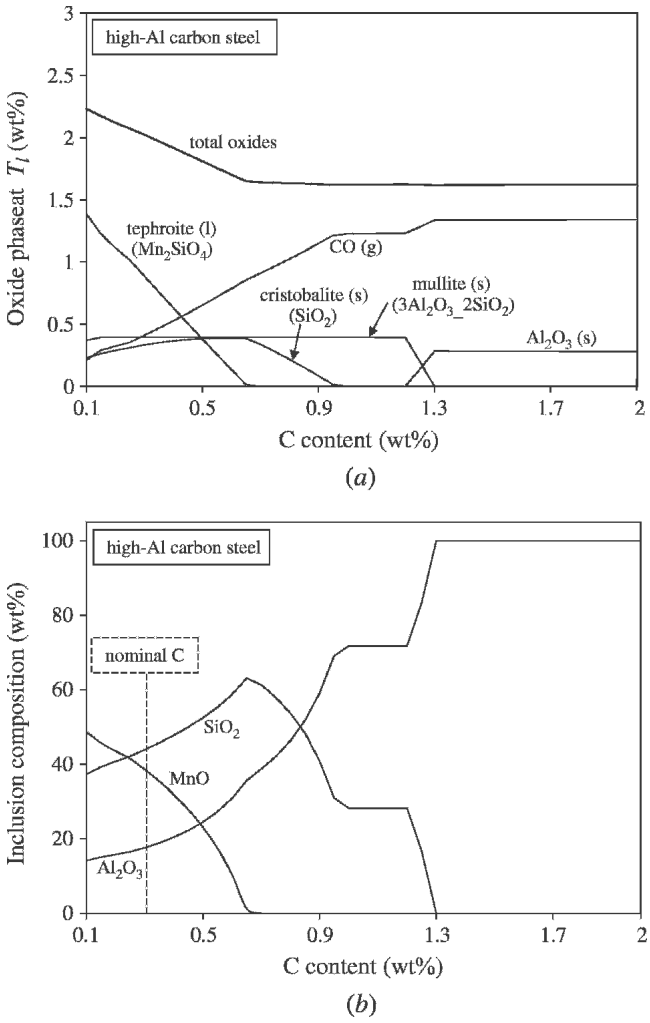

Fig. 10—Effect of the C content on the oxide mass percentages at the liquidus temperature and on the inclusion composition for high-Al carbon steel (ΔC^O = 0.9 wt pct). (*a*) Mass percentage of oxide phases at the liquidus temperature (1528 °C, lever rule). (*b*) Inclusion composition.

tephroite percentage increases strongly with increasing Mn content (Figure 7(b)). It is also possible that the oxygen absorption rate changes with the Mn content in the steel, perhaps due to changes in the CO gas formation, as shown in Figure 7(a).

Figure 8 shows the variations in the predicted oxide percentages at the liquidus temperature (Figure 8(a)) and inclusion composition (Figure 8(b)) with the Si content increasing from 0.1 to 1.0 wt pct. In this and several subsequent figures, the nominal alloy element content is indicated as a vertical dashed line; thus, at this weight percentage, the predicted and measured inclusion compositions agree. As opposed to the effect of Mn in Figure 7(a), it can be seen from Figure 8(a) that the total mass of oxides (per mass of steel) decreases slightly with increasing Si content. This can be attributed to the molecular weight of Mn being almost twice that of Si. The percentages of CO gas and liquid tephroite (Mn_2SiO_4) decrease with increasing Si content, and above about 0.8 wt pct Si, all oxides are predicted to be in the solid state at the liquidus temperature. The calculated inclusion compositions in Figure 8(b) show that the increase in the SiO_2 content with increasing Si is fully at the expense of the MnO content, while the Al_2O_3 percentage is relatively constant. Above 0.8 wt pct Si, MnO is completely absent from the reoxidation inclusions, such that they consist of SiO_2 and Al_2O_3 only, and the inclusion composition becomes independent of the Si content.

Figure 9(a) investigates the effect of the Al content on oxide formation. As expected, the percentage of alumina (Al_2O_3) increases with increasing Al content. All other oxide phase fractions decrease slightly, since the total amount of oxygen absorbed is fixed. The plot of the inclusion composition in Figure 9(b) indicates that the SiO_2 content is relatively unaffected by the Al content, and that the increase in the Al_2O_3 content is mostly accommodated by a decrease in the MnO percentage.

Finally, Figure 10 illustrates the effect of the carbon (C) content. As the C content increases from 0.1 wt pct the total mass of the oxides (per mass of steel) first decreases and then reaches a constant value at about 0.7 wt pct C (Figure 10(a)). The liquid tephroite percentage at the liquidus temperature decreases steeply with increasing C content

and vanishes completely at about 0.7 wt pct C. No other liquid phase is present at higher C contents. The CO gas percentage increases almost linearly with increasing C content, until it reaches an approximately constant value at around 1.0 wt pct C (Figure 10(a)). The CO gas percentage increases at the expense of the solid and liquid oxides, since the total mass of the oxides decreases or remains constant. This indicates that the mass of the (solid) inclusions that are finally formed decreases strongly with increasing C content (up to about 1.0 wt pct), since the CO gas will escape. The calculated inclusion composition as a function of the C content is shown in Figure 10(b). Below 0.7 wt pct C, the MnO percentage decreases and the SiO_2 and Al_2O_3 percentages increase with increasing C content. Between 0.7 and 1.3 wt pct C, the inclusion consists of SiO_2 and Al_2O_3 only. However, the SiO_2 content decreases in this range, and above 1.3 wt pct C, the inclusion consists of Al_2O_3 only. This is possible because most of the absorbed oxygen reacts with the carbon (Figure 10(a)). Obviously, such high C contents are not used in cast steels, but the trends are nonetheless interesting.

2. *Low-Al carbon steel*

A separate set of experiments were conducted by Lyman and Boulger[18] for low-Al carbon steel, where the Al content was only 0.05 wt pct (Table I). The nominal Mn content was 0.4 wt pct, as opposed to the 0.8 wt pct for the high-Al steel of Section IV–A–1. Figures 11(a) and (b) show the predicted variation of the oxide mass percentages at the liquidus temperature and the inclusion composition, respectively, as a function of the percentage of absorbed oxygen, ΔC^O. This figure is analogous to Figure 6 for the high-Al carbon steel. Figure 11(b) is used to determine the mass of absorbed oxygen, ΔC^O, by matching the measured and predicted inclusion compositions. In this case, the data points were shifted along the horizontal axis until the measured SiO_2 content fell exactly on the curve representing the predicted SiO_2 content. Interestingly, the same $\Delta C^O = 0.9$ wt pct value is obtained as for the high-Al carbon steel (Figure 6(b)). With that value for ΔC^O, the measured and predicted Al_2O_3 and MnO + FeO contents also agree very well. Note that the Al_2O_3 content in the inclusion is much lower for the present low-Al carbon steel than for the high-Al carbon steel (Figure 6(b)). The match in Figure 11(b) is unique in that no other ΔC^O would result in a match of all inclusion oxide percentages.

Figure 12 investigates the effect of the Mn content in the low-Al carbon steel on the oxide formation and inclusion composition, with ΔC^O kept constant at 0.9 wt pct. This figure is similar to Figure 7 for the high-Al carbon steel. The inclusion composition measurements of Lyman and Boulger[18] are indicated as symbols in Figure 12(b) and correspond to Mn contents of 0.4 wt pct (nominal), 0.8 wt pct, 1.6 wt pct, and 3.0 wt pct. Overall, the trends observed in the measured data are predicted correctly. The MnO content increases, the SiO_2 content decreases, and the Al_2O_3 content is approximately constant with increasing Mn content. Above 1.6 wt pct Mn, the inclusion composition becomes independent of the Mn content. Some disagreement between the measured and predicted inclusion compositions exists at the two higher Mn contents (1.6 and 3.0 wt pct), as already observed in Section IV–A–1 for the high-Al carbon steel. As discussed in connection with Figure 7(b), no definite conclusions can be drawn with respect to the origin of the differences. Some of the disagreement may be attributed to uncertainties in the experimental data. For example, with increasing Mn content, the measured SiO_2 content in the inclusions first decreases, then increases (at 1.6 wt pct Mn), and finally decreases again. If one ignores the three samples at 1.6 wt pct Mn, the trends are in much better agreement. Despite these uncertainties, the comparisons provide additional confidence in the present method for calculating the reoxidation inclusion composition.

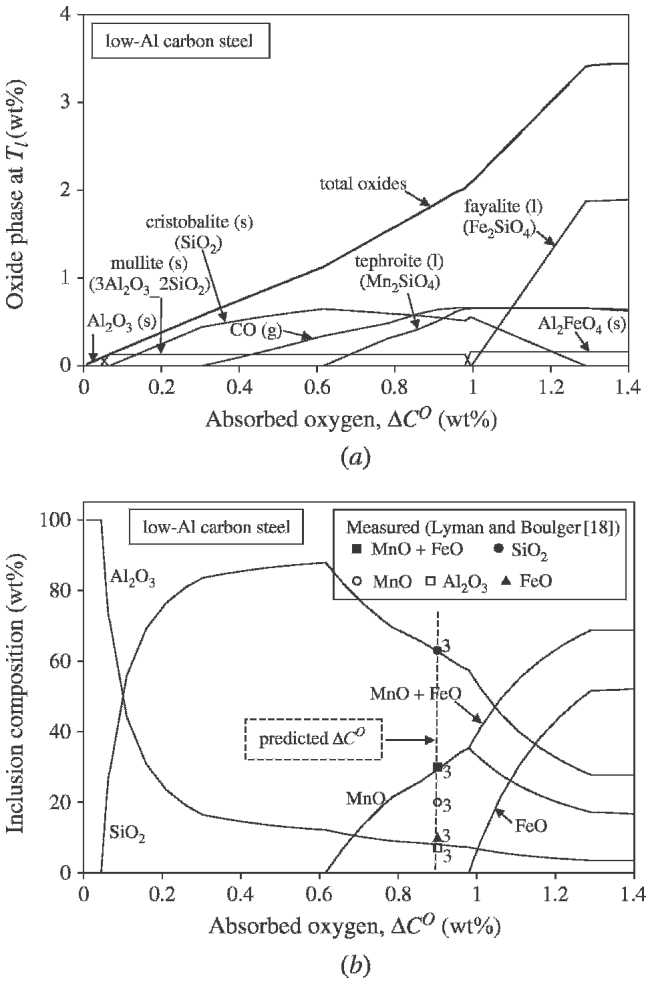

Fig. 11—Effect of the mass percentage of absorbed oxygen on the oxide mass percentages at the liquidus temperature and on the inclusion composition for low-Al carbon steel. (*a*) Mass percentage of oxide phases at the liquidus temperature (1528 °C, lever rule). (*b*) Inclusion composition (numbers next to symbols indicate number of samples).

B. *Alloy Steel*

Griffin and Bates[19,20] optically and chemically analyzed macroinclusions from both low-alloy and high-alloy steel castings. The measurements of reoxidation inclusion composition used in the following are from test plates that were cast in both sand and special ceramic molds. The geometry of the test plate is shown in Figure 13. The pouring weight

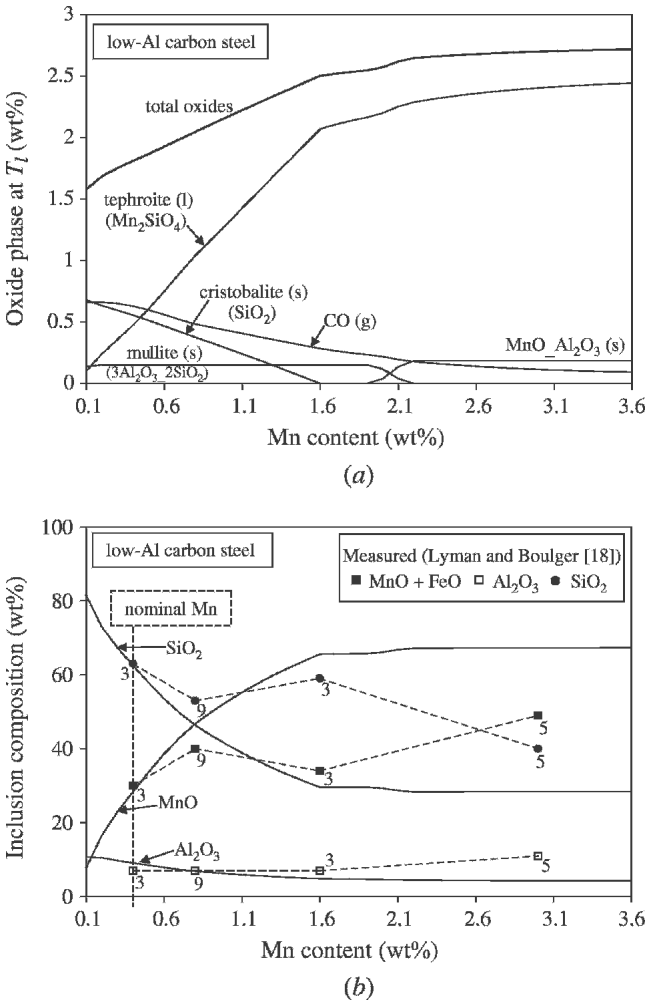

Fig. 12—Effect of the Mn content on the oxide mass percentages at the liquidus temperature and on the inclusion composition for low-Al carbon steel (ΔC^O = 0.9 wt pct). (*a*) Mass percentage of oxide phases at the liquidus temperature (1528 °C, lever rule). (*b*) Inclusion composition (numbers next to symbols indicate number of samples).

of the plate was approximately 90.7 kg (200 lb) and the casting weight was about 43.1 kg (95 lb). The pouring temperature was about 1600 °C.

From among the steels investigated by Griffin and Bates,[19,20] one low-alloy and one high-alloy steel were selected for analysis here. Their nominal compositions are provided in Table I. The high-alloy steel designation is CF8M (Alloy Casting Institute). The reoxidation inclusion compositions measured by Griffin and Bates[19,20] for these two steels are summarized in Tables IV and V. For the low-alloy steel (Table IV), both matrix phase and bulk inclusion compositions are provided. They differ primarily in the Al_2O_3 content. For the matrix phase, the Al_2O_3 content is relatively constant for all eight specimens, with the average equal to 22 wt pct; this matrix phase is likely to be the actual reoxidation product. On the other hand, the bulk Al_2O_3 contents in Table IV vary strongly and are, on average, much higher (about 60 pct). The higher bulk Al_2O_3 content may be explained by the presence of Al_2O_3 deoxidation particles inside the reoxidation inclusions. These deoxidation inclusions are already present in the steel in the ladle. They may be captured by the rapidly moving, partially liquid reoxidation inclusions during filling.[4] The strong variations in the bulk Al_2O_3 content may be due to the eight specimens being from different test plates that were poured under different conditions and from heats with different deoxidation practices. This issue is further

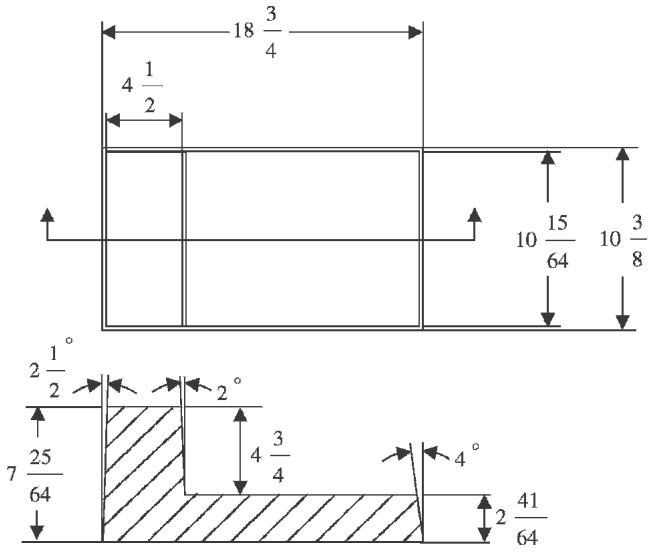

Fig. 13—Geometry of the low- and high-alloy steel test plate castings;[19,20] the unit for all lengths is inches.

Table IV. Measured Matrix Phase and Bulk Inclusion Compositions for Low-Alloy Steel (Weight Percent)[20]

	Matrix Phase				Bulk Inclusion			
Specimen	Al_2O_3	SiO_2	MnO	CaO	Al_2O_3	SiO_2	MnO	CaO
103-4	24	45	20	6	42	36	15	4
106-116-2	26	42	28	5	74	15	9	2
107-103-3	18	46	36	0	61	22	16	0
109-119-4	22	43	28	5	64	26	10	1
110-107-2	19	49	28	0	75	16	8	0
110-135	19	48	29	2	61	22	16	1
111-24	20	55	20	3	65	26	7	1
112-5	25	42	34	0	40	35	25	0
Average	22	46	28	3	60	25	13	1

Table V. Measured Inclusion Compositions for High-Alloy Steel, CF8M (Weight Percent)[19]

Specimen	SiO_2	Cr_2O_3	MnO	FeO	TiO_2	Al_2O_3
113-25	53	31	16	0	0	1
113-26	59	24	14	0	4	0
113-28	60	18	18	0	0	2
114-4	59	30	11	0	0	0
114-5	55	38	5	2	0	0
114-6	62	28	7	3	0	0
114-8	60	27	10	2	0	2
114-109-1	66	23	11	0	0	0
114-110-2	63	27	10	0	0	0
114-138-2	71	17	9	2	0	0
Average	60.8	26.3	11.1	0.9	0.4	0.5

addressed subsequently. No such distinction between matrix and bulk inclusion compositions is necessary for the high-alloy steel.[19] The compositions of the ten inclusion specimens listed in Table V for the CF8M steel are all relatively similar. These inclusions are believed to be reoxidation products.[19]

1. *Low-alloy steel*

Figure 14 shows the effect of the mass of absorbed oxygen, ΔC^O, on oxide formation and inclusion composition for the low-alloy steel. This figure is similar to Figures 6 and 11 for the carbon steels, and the reader is referred to in Section IV–A for a more detailed discussion. The main difference from these earlier figures is that for the low-alloy steel a Cr containing oxide forms for ΔC^O greater than about 1.1 wt pct (Figure 14(a)). In the same manner as in Section IV–A, Figure 14(b) is used to determine the mass of absorbed oxygen, ΔC^O, by matching the measured and predicted inclusion compositions. According to the preceding discussion, the average matrix phase composition in Table IV represents the measured reoxidation inclusion composition. Note that no FeO was detected in the inclusions (Table IV); hence, the MnO and FeO percentages do not need to added as was done for the carbon steels. The measured CaO content (3 wt pct) is neglected. Figure 14(b) shows that $\Delta C^O = 0.9$ wt pct provides a good match between the measured and predicted inclusion compositions. The matching was performed based on the SiO_2 and MnO contents only. The measured Al_2O_3 content of 22 wt pct was primarily used to determine the Al content in the steel, because the Al content was not provided by Griffin and Bates.[20] The resulting value of 0.2 wt pct Al (Table I) is realistic. The good match observed in Figure 14(b) provides increased confidence in the present method for determining the inclusion composition, since there is no uncertainty due to the FeO content as for the carbon steel. Interestingly, the 0.9 wt pct value for the mass of absorbed oxygen is the same as was determined for the carbon steels.

With an Al_2O_3 content of 22 pct in the matrix phase created by reoxidation, the measured Al_2O_3 bulk inclusion percentages can be used to back out the mass percentage of deoxidation inclusions for each of the specimens in Table IV. The result is shown in Figure 15. It can be seen that between 0.5 and 4 wt pct Al_2O_3, deoxidation inclusions must be present in the steel to explain the high values of the measured Al_2O_3 bulk inclusion percentages. For example, a measured Al_2O_3 content of 60 wt pct in the bulk inclusion corresponds to 2 wt pct Al_2O_3 in the steel before any oxygen is added. Such high deoxidation inclusion weight percentages are not realistic. The high values imply that the solid Al_2O_3 deoxidation inclusions are not uniformly distributed in the liquid steel. Most likely, deoxidation inclusions are captured by the partially liquid reoxidation inclusions during filling, as mentioned previously. This effect is not easily incorporated in the present model. Nonetheless, it is useful to see from Figure 15 that the measured variations in the SiO_2 and MnO bulk inclusion percentages can be explained by the presence of Al_2O_3 deoxidation inclusions.

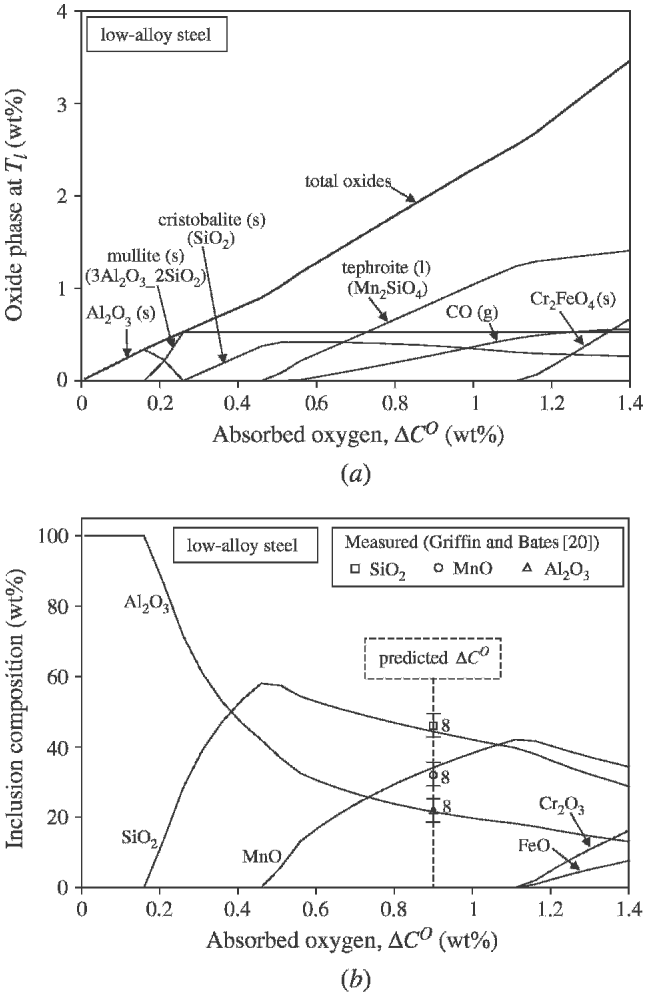

Fig. 14—Effect of the mass percentage of absorbed oxygen on the oxide mass percentages at the liquidus temperature and on the inclusion composition for low-alloy steel. (*a*) Mass percentage of oxide phases at the liquidus temperature (1528 °C, lever rule). (*b*) Inclusion composition (numbers next to symbols indicate number of samples).

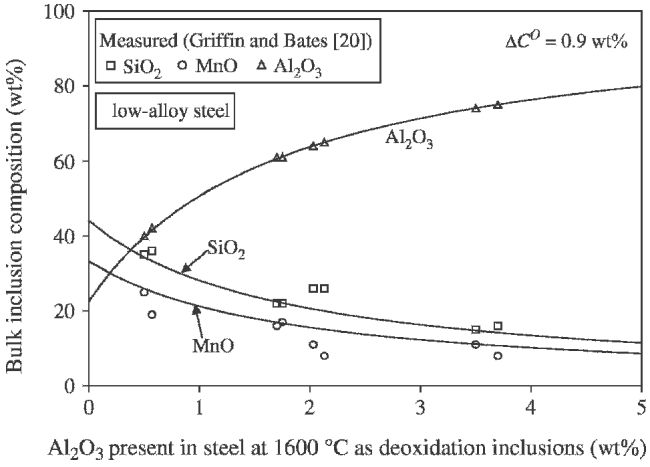

Fig. 15—Effect of the mass percentage of Al_2O_3 deoxidation inclusions on the bulk composition of the reoxidation inclusions in low-alloy steel.

2. *High-alloy steel (CF8M)*

Figure 16 shows the predicted variation of the oxide percentages in the high-alloy steel (CF8M; Table I) with temperature, for the lever rule approach and an absorbed oxygen mass of 0.9 wt pct. The nominal Si content of 1.33 wt pct in Table I was not reported by Griffin and Bates.[19] The method used to determine both the Si content and the mass of absorbed oxygen is explained subsequently in connection with Figure 17. It can be seen from Figure 16(a) that solid cristobalite (SiO_2) is the first oxide to form as the temperature decreases from 1600 °C. At about 1500 °C, all of the Si is oxidized, and solid Cr_2O_3 starts to form. At about 1470 °C, the cristobalite is transformed into tridymite (SiO_2), and at the liquidus temperature, the Cr_2O_3 mass fraction reaches a maximum. No manganese-containing, liquid or gaseous oxides (*e.g.,* CO) are present at the liquidus temperature. Below the liquidus temperature (Figure 16(b)), the SiO_2 mass fraction increases at the expense of Cr_2O_3, and at slightly below 900 °C, all of the Cr_2O_3 is decomposed. Also, the tridymite (SiO_2) is transformed into quartz (SiO_2). At about 700 °C, Mn is starting to oxidize by forming solid tephroite (Mn_2SiO_4). Finally, at about 300 °C, some of the quartz (SiO_2) and all of the tephroite (Mn_2SiO_4) are consumed to form solid Mn_2O_2_ SiO_2. Again, the numerous solid-state transformations predicted by the lever rule method as room temperature is approached are unlikely to be completed due to the slow rate of mass diffusion in the solid. Although no Mn oxides are present at the liquidus temperature, Figure 16 shows that it is thermodynamically possible for Mn oxides to be present at room temperature.

Figure 17 shows the calculated variation of the inclusion composition with Si content (Figure 17(a)) and ΔC^O (Figure 17(b)). These inclusion compositions were obtained using the same conversion method as explained previously in connection with the carbon steels. It can be seen from Figure 17(a) that below about 0.65 wt pct Si, the inclusions are predicted to consist entirely of Cr_2O_3. For larger Si contents, the SiO_2 percentage in the inclusions increases at the expense of Cr_2O_3. For Si contents above about 1.6

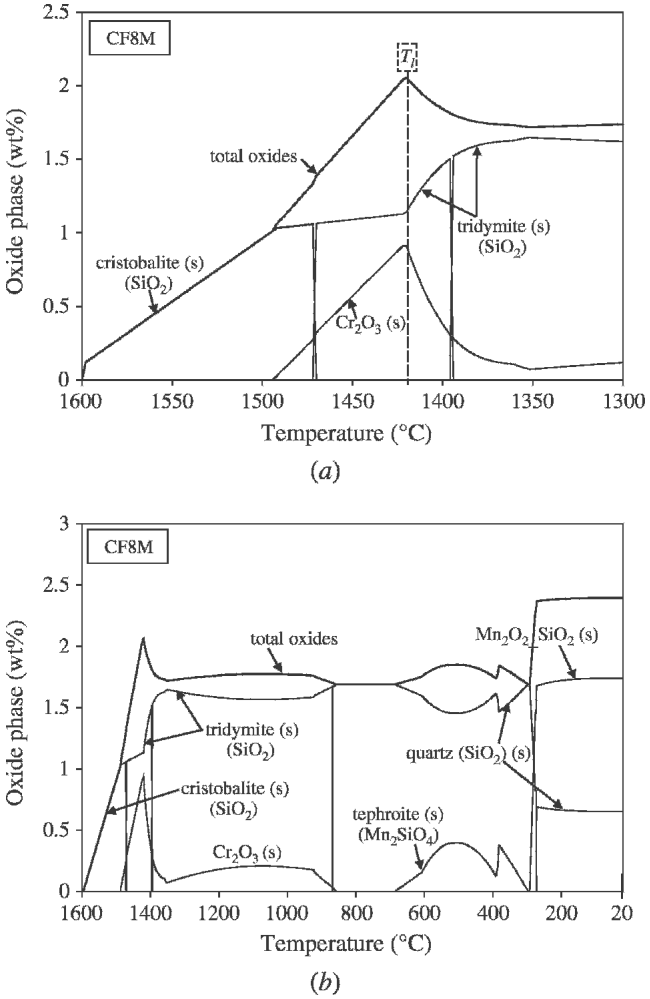

Fig. 16—Evolution of the mass percentage of the various oxide phases in high-alloy CF8M steel calculated using the lever rule method (ΔC^O = 0.9 wt pct). (*a*) Temperature range: 1600 °C to 1300 °C. (*b*) Temperature range: 1600 °C to 20 °C.

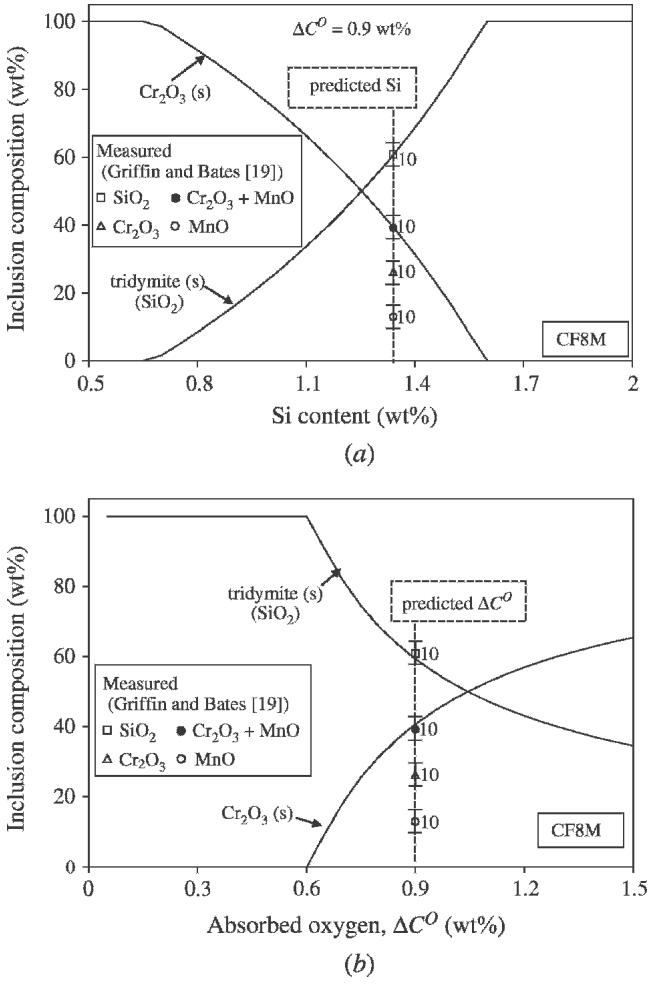

Fig. 17—Effect of the Si content and the mass percentage of absorbed oxygen on the inclusion composition for high-alloy CF8M steel (numbers next to symbols indicate number of samples). (*a*) Effect of Si content for ΔC^O = 0.9 wt pct. (*b*) Effect of mass percentage of absorbed oxygen for a Si content of 1.33 wt pct.

wt pct, the inclusions consist entirely of SiO_2. Figure 17(b) shows that for ΔC^O below 0.6 wt pct, the inclusions are also predicted to be 100 pct SiO_2. For larger ΔC^O, the Cr_2O_3 content increases at the expense of SiO_2.

The mass of absorbed oxygen, ΔC^O, and the Si content in the CF8M steel are both determined by matching the measured and predicted inclusion compositions. The average values in Table V are used as the measured composition, neglecting the small percentages of FeO, TiO_2, and Al_2O_3. Table V shows that the inclusions analyzed by Griffin and Bates[19] contained, on average, about 11 wt pct MnO. Unfortunately, as shown in Figure 17, no MnO is predicted to be present in the inclusions using the present conversion method. However, as explained in connection with Figure 16, it is possible for Mn oxides to form in the solid state as room temperature is approached. The lever rule predictions in Figure 16 also show that it is possible for the Cr_2O_3 to be decomposed at lower temperatures. These solid-state transformations are not modeled in the current study. Nonetheless, based on this discussion, it appears to be reasonable to add the measured MnO and Cr_2O_3 percentages and compare them to the predicted Cr_2O_3 percentage. A series of calculations were performed where both ΔC^O and the Si content were varied (not shown here), until the predicted SiO_2 and Cr_2O_3 percentages matched with the measured SiO_2 and MnO + Cr_2O_3 percentages, respectively. A unique match was obtained for ΔC^O = 0.9 wt pct and a Si content of 1.33 wt pct, as shown in Figure 17. This Si content is reasonable for CF8M steel. Interestingly, the obtained value of 0.9 wt pct for the mass of absorbed oxygen is the same as found for the carbon and low-alloy steels.

For completeness, the effects of variations in the Mn and Cr content on the inclusion composition for the CF8M steel are shown in Figures 18(a) and (b), respectively. Within the range of 0.5 to 1.5 wt pct plotted in Figure 18(a), the Mn content does not appear to have a strong influence on the inclusion composition. On the other hand, increasing the Cr content from 18 to 21 wt pct causes a significant increase in the Cr_2O_3 content in the inclusions from about 30 to 55 pct, with the SiO_2 content decreasing proportionally (Figure 18(b)).

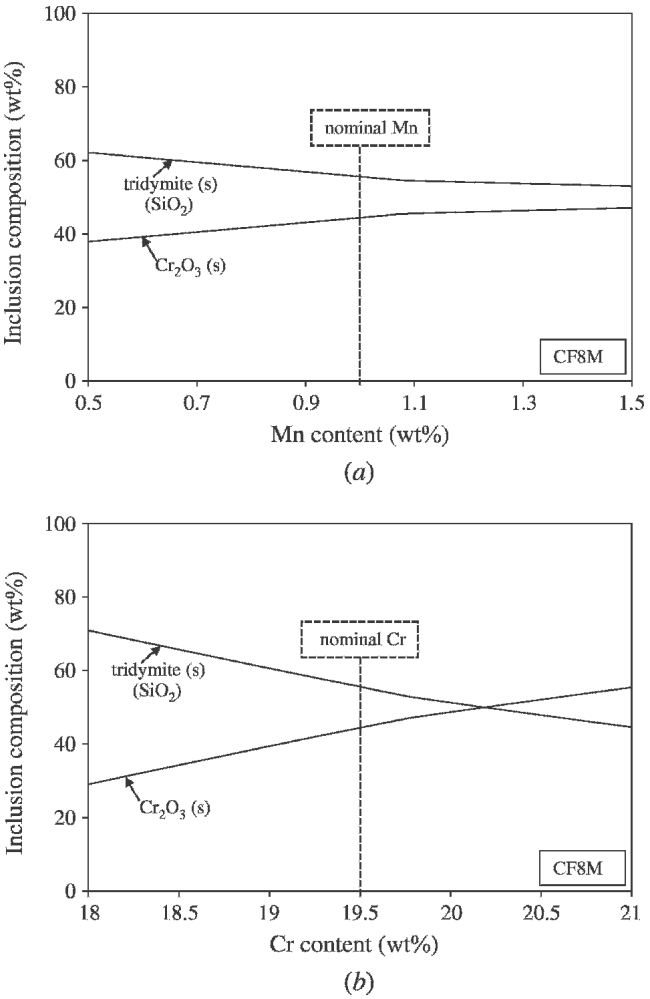

Fig. 18—Effect of the Mn and Cr contents on the inclusion composition for high-alloy CF8M steel (ΔC^O = 0.9 wt pct). (*a*) Effect of Mn content. (*b*) Effect of Cr content.

V. DISCUSSION OF OXYGEN ABSORPTION RATE

The results in Section IV show that, despite some uncertainties, the composition of reoxidation inclusions in casting of carbon and low-/high-alloy steels can be successfully predicted using the present approach. The inclusion composition was found to be very sensitive to the amount of oxygen absorbed by the steel. Interestingly, for all experiments analyzed in the current study, the matching of measured and predicted inclusion compositions resulted in the same value (*i.e.,* 0.9 wt pct) for the mass of absorbed oxygen per mass of steel, ΔC^O. Thus, the main questions remaining are why ΔC^O is the same for all cases analyzed here and how the value of 0.9 wt pct can be achieved. The oxygen absorption can generally be expected to depend on the pouring conditions (*e.g.,* size and position of ladle), the casting system design (*e.g.,* height of sprue, design of gates, and runners), and numerous other factors. While the casting trials of Lyman and Boulger[18] and Griffin and Bates[19,20] were not exactly the same, all of them involved plates of similar size that were cast using a relatively ''standard'' filling system (*i.e.,* steel is poured from a ladle into a vertical sprue with a fall height of about 1 m). This similarity may explain why ΔC^O was the same for these casting trials. If the plates had been cast using a vacuum-assisted countergravity pouring system, for example, ΔC^O may be lower and the inclusion composition would have been different.

In order to better understand how a value of 0.9 wt pct for ΔC^O can be achieved, the following order-of-magnitude estimate of ΔC^O can be made based on Eq. [4]. Assume, as an extreme case, that the steel being poured from the ladle into the mold consists of a stream of small spherical droplets of average radius *r.* Such a situation could arise if the stream is highly fragmented by a poor nozzle design (for a bottom-pour ladle) or by excessive splashing. As illustrated in Figure 19(a), each droplet can be thought of as being exposed to air flowing over it with a certain relative velocity u_a. For spherical droplets, the ratio of the surface area to the mass is given by

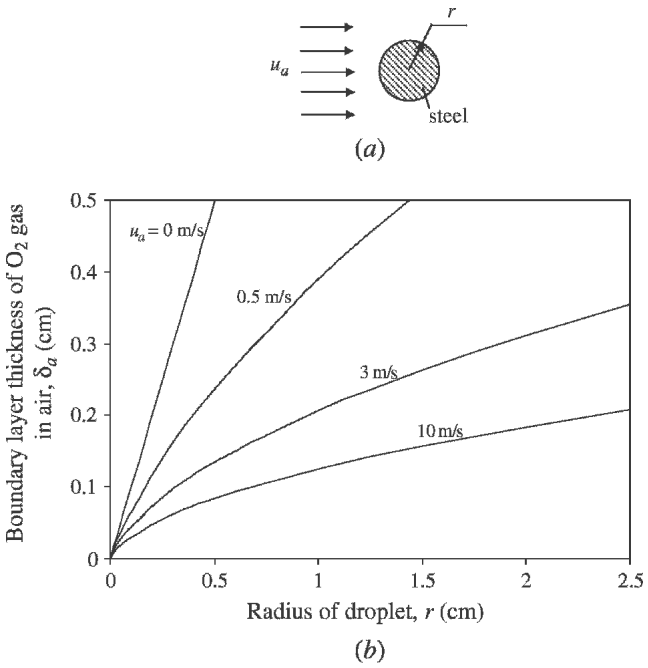

Fig. 19—Oxygen transfer from air to a droplet of steel. (*a*) Schematic illustration of air flowing past a steel droplet. (*b*) Boundary layer thickness of O_2 gas in air as a function of droplet radius and relative velocity.

$$\frac{A_s}{m_s} = \frac{3}{\rho_s r} \qquad [6]$$

where ρ_s is the steel density taken as 6.8 g/cm^3. Substituting Eq. [6] into Eq. [4] and integrating Eq. [4] over the time the droplet is exposed to air, t_e, yields the following expression for the mass fraction of absorbed oxygen:

$$\Delta C^{\mathrm{O}} = \frac{6M^{\mathrm{O}}}{\rho_s r}\frac{D_a^{\mathrm{O}_2}}{\delta_a^{\mathrm{O}_2}}\frac{p_a^{\mathrm{O}_2}}{\mathrm{R}T}t_e \qquad [7]$$

During integration, all variables on the right-hand side of Eq. [4] were assumed constant. The mass diffusivity of O_2 in air, $D_a^{\mathrm{O}_2}$, at 1600 °C is equal to 4.56 cm^2/s[21] and the partial pressure of O_2 in air, $p_a^{\mathrm{O}_2}$, is equal to 21.23 kPa. Equation [7] shows that the mass fraction of oxygen absorbed by the steel droplet is proportional to the O_2 partial pressure and the exposure time and inversely proportional to the droplet radius and the boundary layer thickness.

The O_2 gas concentration boundary layer thickness, $\delta_a^{\mathrm{O}_2}$, is a function of the relative velocity between the droplet and the air, u_a, the droplet radius, and various air properties. This thickness can be estimated from the Ranz–Marshall correlation[22] for convective mass transfer, *i.e.*,

$$\mathrm{Sh} = 2 + 0.6\mathrm{Re}^{1/2}\mathrm{Sc}^{1/3} \qquad [8]$$

where Sh is the Sherwood number $(\mathrm{Sh} = 2r/\delta_a^{\mathrm{O}_2})$, Re is the Reynolds number $(\mathrm{Re} = 2r\rho_a u_a/\mu_a)$, and Sc is the Schmidt number $(\mathrm{Sc} = \mu_a/(\rho_a D_a^{\mathrm{O}_2}))$. The density, ρ_a, and the dynamic viscosity, μ_a, of air at 1600 °C are approximately equal to 0.19×10^{-3} g/cm^3 and 5.96×10^{-4} g/(cm · s), respectively.[23] The variation of the boundary layer thickness calculated from Eq. [8] as a function of the droplet radius and the relative velocity between the droplet and the air is plotted in Figure 19(b). For $u_a = 0$, $\delta_a^{\mathrm{O}_2}$ is equal to r. For sufficiently large Reynolds numbers, the boundary layer thickness increases with droplet radius according to $\delta_a^{\mathrm{O}_2} \sim r^{1/2}$, and decreases with increasing relative velocity according to $\delta_a^{\mathrm{O}_2} \sim u_a^{-1/2}$. As a specific example, for a droplet radius of 1 cm and a relative velocity of 4.5 m/s, the boundary layer thickness is equal to about 0.15 cm.

Applying the above equations to the previous example of a stream of droplets, the following conservative estimates can now be made. For a typical fall height of the liquid steel from the ladle into the mold of about $h = 1$ m, an estimate of the relative velocity between the droplets and the air is then given by $u_a = \sqrt{2gh} \approx 4.5$ m/s, where $g = 9.81$ m/s^2. Considering this velocity and the distances involved, an upper limit on the exposure time can be taken as $t_e = 1$ second. The entire fill time of a mold, which is typically much longer than 1 second, cannot be taken as the exposure time, because the steel cannot be assumed to consist of droplets once it is deeper inside the mold. With these values for u_a and t_e, Eqs. [7] and [8] can be solved simultaneously for the boundary layer thickness and the droplet radius that are needed to achieve a mass percentage of absorbed oxygen, ΔC^{O}, of 0.9 wt pct. The result is $\delta_a^{\mathrm{O}_2} = 0.07$ cm and $r = 0.1$ cm. In other words, the liquid metal stream from the ladle into the mold would need to consist of 2 mm diameter droplets to absorb sufficient oxygen in 1 second that the observed reoxidation inclusion compositions are attained. Note that in this extreme example all of the steel (*i.e.,* the entire droplet) is assumed to achieve $\Delta C^{\mathrm{O}} = 0.9$ wt pct of absorbed oxygen.

If the steel during pouring flows in a more compact manner, such as in a cylindrical jet rather than a stream of small droplets, the absorbed oxygen is not likely to be uniformly distributed in the liquid steel. Instead, the oxidation would be limited to a relatively thin layer of liquid steel adjacent to the free surface, as illustrated in Figure 20(a). In this alternative scenario, the 0.9 wt pct value for the mass percentage of oxygen is only achieved in the thin oxidation layer, the reoxidation inclusions only form in this layer, and the liquid steel outside of the layer is unaffected. Then, the mass of steel, m_s, in Eq. [4] is not equal to the total mass of steel poured, but only equal to the mass of the steel in the oxidation layer. An effective thickness of the oxidation layer, d_s^{ox}, may be estimated as follows. Assuming the oxidation layer to be approximately flat, the ratio of the surface area to the mass of the steel in the oxidation layer is given by

$$\frac{A_s}{m_s} = \frac{1}{\rho_s d_s^{ox}} \qquad [9]$$

Substituting Eq. [9] into Eq. [4] and performing the same kind of integration as was done in connection with Eq. [7] yields the following expression for the thickness of the oxidation layer:

$$d_s^{ox} = \frac{2M^{\mathrm{O}}}{\rho_s \Delta C^{\mathrm{O}}}\frac{D_a^{\mathrm{O}_2}}{\delta_a^{\mathrm{O}_2}}\frac{p_a^{\mathrm{O}_2}}{\mathrm{R}T}t_e \qquad [10]$$

The oxidation layer thickness calculated from Eq. [10] as a function of the exposure time, t_e, is plotted in Figure 20(b)

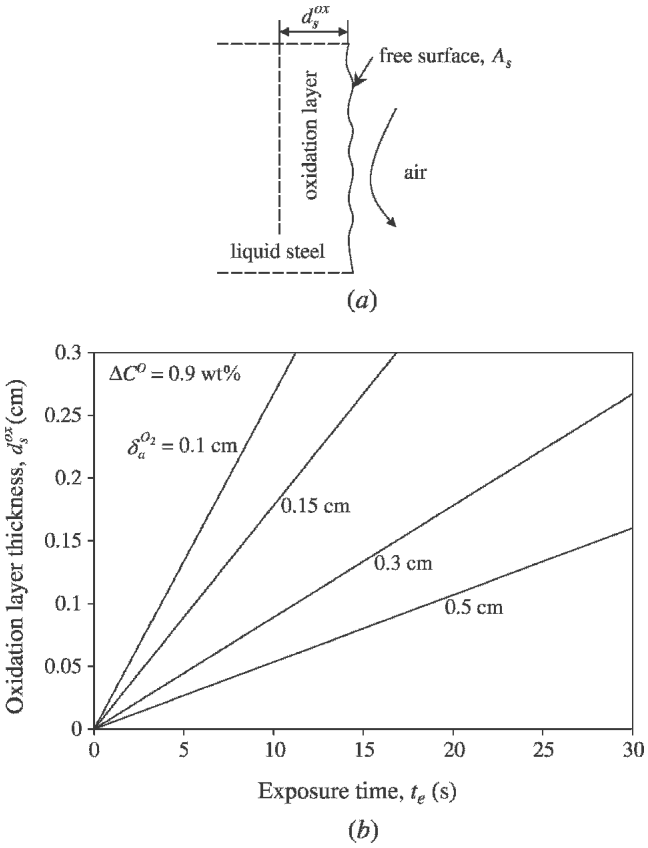

Fig. 20—Oxidation layer adjacent to the free surface of the steel in which the mass percentage of absorbed oxygen reaches 0.9 wt pct. (*a*) Schematic illustration of the oxidation layer. (*b*) Oxidation layer thickness as a function of exposure time and O_2 gas boundary layer thickness.

for $\Delta C^{O} = 0.9$ wt pct and the boundary layer thickness, $\delta_a^{O_2}$, ranging from 0.1 to 0.5 cm. It can be seen that, as expected, the thickness d_s^{ox} of the layer where a mass fraction of 0.9 wt pct of oxygen is achieved increases linearly with the exposure time. Also, d_s^{ox} increases with decreasing $\delta_a^{O_2}$ (or increasing oxygen transfer rate through the air). The correlation for the boundary layer thickness around a sphere (Eq. [8]) is approximately valid for other flow geometries, including a cylindrical stream. For example, for a stream of 2.5 cm radius and a relative velocity of 4.5 m/s, $\delta_a^{O_2}$ may be estimated from Figure 19(b) to be about 0.3 cm. Then, Figure 20(b) shows that the oxidation layer reaches a thickness of 0.1 mm after 1 second of exposure time and 1 mm after 10 seconds. Hence, regardless of the exact exposure time and flow conditions, a large portion of a compact metal stream would be unaffected by oxygen absorption.

The previous two order-of-magnitude estimates represent only limiting cases for achieving the 0.9 wt pct of absorbed oxygen that results in the measured and predicted reoxidation inclusion compositions to agree. They show that depending on the flow conditions, the oxygen and, hence, the inclusions may be distributed nonuniformly in the liquid steel. Therefore, in order to truly predict the inclusion composition, the complex internal transport of chemical species in the liquid steel together with the formation of the inclusions would have to be modeled in detail. The preceding discussion shows that such a model would need to resolve the transport processes on a submillimeter scale. This would be difficult to accomplish on the scale of an entire casting.

VI. CALCULATION OF REOXIDATION RATES

The present model for the oxygen absorption rate (Section II), together with the knowledge of the reoxidation inclusion composition (Sections III and IV), allows for the calculation of the rates at which the alloying elements in the steel (and the oxygen) are consumed and at which the inclusions are formed. Assuming a constant boundary layer thickness, equal to some average value, and constant properties, and neglecting $p_{as}^{O_2}$ as before, Eq. [2] can be integrated over time to yield the following expression for the number of moles of absorbed oxygen

$$n^{O} = 2\frac{D_a^{O_2}}{\delta_a^{O_2}}\frac{p_a^{O_2}}{RT}(\bar{A}_s t_e) \qquad [11]$$

where the product of the average free surface area of the liquid steel and the exposure time, $(\bar{A}_s t_e)$, is given by

$$\bar{A}_s t_e = \int A_s(t)dt \qquad [12]$$

This area integral could, in principle, be obtained from the results of computer simulations of the filling process of a casting, such as those performed by virtually all commercially available casting simulation software. The integration limits would then correspond to the entire fill time of a casting. Care should be taken to include the metal stream between the ladle and the mold, since considerable reoxidation of the steel can already occur in this generally unprotected portion of the flow. It should, however, be noted that the lack of numerical resolution in current filling simulations could cause a severe underestimation of the free surface area, especially if the flow is highly fragmented and turbulent.

The only other factor in Eq. [11] that is generally unknown is the boundary layer thickness of the oxygen in the air, $\delta_a^{O_2}$. To a good approximation, $\delta_a^{O_2}$ can be calculated from the mass-transfer correlation given by Eq. [8], as a function of the free surface geometry (*e.g.,* the radius, *r*, of the stream or of a droplet) and the relative velocity between the steel and the air, u_a, as shown in Figure 19(b). The boundary layer thickness can be expected to vary considerably with location in the flow and time during filling. Hence, the results of a filling simulation could be used to evaluate $\delta_a^{O_2}$ instantaneously at all points on the free surface. In that case, $\delta_a^{O_2}$ should be included in the integration represented by Eq. [12]. By performing these calculations as part of a filling simulation, the effects of the pouring and gating system design on the oxygen absorption (and, hence, inclusion formation) could be investigated numerically.[4]

For the purpose of the present calculations, a representative average value for $\delta_a^{O_2}$ is estimated from Figure 19(b) as follows. A lower bound on the liquid steel velocity may be taken as 1 m/s (corresponding to a fall height of only 5 cm). The velocity in typical steel casting operations will generally not exceed 10 m/s. Furthermore, due to surface tension, the free surface structures are typically not smaller than about 0.1 cm in the radius of curvature. Due to continual

breakup of the streams, an upper bound on the radius in steel casting may be around 2.5 cm (1 in.). Note that for these ranges of velocities and radii, the boundary layer thickness is not a strong function of the radius. In view of Figure 19(b), a representative average value for $\delta_a^{O_2}$ can then be taken as 0.15 cm (corresponding, for example, to $r = 1$ cm and $u_a = 5$ m/s).

Since all of the absorbed oxygen is consumed in the formation of inclusions, the knowledge of the number of moles of oxygen absorbed, n^O, from Eq. [11] allows for the calculation of the mass of the individual oxides formed. This is straightforward, since the composition of the inclusions and the molecular weights of the oxides are known. Also, the mass of the alloying elements in the steel that are consumed in the oxidation reactions can be readily calculated. Furthermore, the volumes of the CO gas formed and of the air needed to supply the oxygen can be calculated from the ideal gas law; the pressure and temperature are simply taken as 1 atm and 25 °C, respectively. It is emphasized that the results of these calculations are a function of the ratio $(\bar{A}_s t_e)/\delta_a^{O_2}$ only (Eq. [11]); they do *not* depend on the mass of absorbed oxygen, ΔC^O, the mass of steel, or the degree of mixing of the oxygen in the steel.

Results for the low-alloy steel (Table I) and $\delta_a^{O_2} = 0.15$ cm are shown in Figure 21. Figure 21 shows that, as expected, the mass of the alloy elements consumed (Figure 21(a)) and of the inclusions formed (Figure 21(b)) increases linearly with the integrated product of the free surface area and the exposure time, $(\bar{A}_s t_e)$. It is important to realize that the same value of $(\bar{A}_s t_e)$ can be achieved for different amounts of steel poured, depending on how fragmented or compact the stream is and how long the free surface is exposed to air. For example, for $(\bar{A}_s t_e) = 100$ m^{2}s (and $\delta_a^{O_2} = 0.15$ cm), 2.5 kg of solid inclusions are formed (Figure 21(b)). This value of $(\bar{A}_s t_e)$ could be achieved for 1 ton of steel if the flow is highly fragmented or the mold filling time is very long, or for 10 tons of steel if the flow is more compact and rapid or the stream is protected. Figure 21 also shows that for every 1 kg of solid reoxidation inclusions formed (corresponding to $(\bar{A}_s t_e) \approx 40$ m^{2}s in Figure 21), 0.2 m^3 of CO gas is produced and almost 2 m^3 of air is needed to supply the oxygen (at 25 °C and 1 atm).

Figure 21 also allows for the integrated free surface area, $(\bar{A}_s t_e)$, to be determined from the knowledge of the mass of the alloy elements consumed. A loss of about 0.73 kg Mn, 0.41 kg Si, 0.41 kg Al, and 0.14 kg C per ton of steel has been reported by Brower *et al.*,[24] for unprotected tapping and ladle filling operations in wrought steel production. These values are indicated in Figure 21(a) as symbols. The symbols were shifted along the horizontal axis until the Mn loss (0.73 kg) agreed with the calculated value. This fit occurs for $(\bar{A}_s t_e) = 110$ m^{2}s. Although the steels investigated by Brower *et al.*[24] had a somewhat different composition than the low-alloy steel to which Figure 21 corresponds, reasonable agreement is achieved for the other consumed elements as well. There is an additional uncertainty of at least a factor of 2 in this value for $(\bar{A}_s t_e)$, because the boundary layer thickness, $\delta_a^{O_2} = 0.15$ cm, for which Figure 21 was plotted represents only a rough estimate (as previously discussed). Considering typical values for the fall height and the velocity of the stream during pouring, the exposure time may be estimated as 1 second

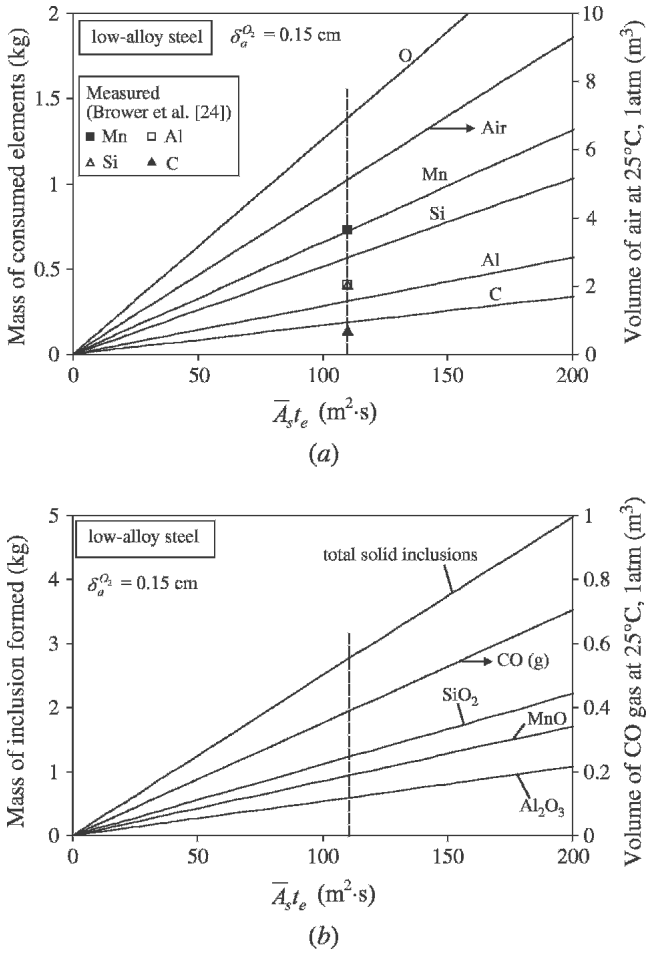

Fig. 21—Mass of consumed alloying elements, volume of air need to supply the oxygen, mass of inclusions formed, and volume of CO gas formed as a function of the integrated free surface area and exposure time product for low-alloy steel ($\delta_a^{O_2} = 0.15$ cm). (*a*) Mass of consumed alloying elements and volume of air. (*b*) Mass of inclusions and volume of CO gas formed.

(note that the exposure time is not directly related to the mass of the steel). With $t_e = 1$ s, the average free surface area that corresponds to the measured alloy element losses would then be equal to 110 m^2. Such a high value for the free surface area indicates the presence of considerable stream roughness, splashing, and air entrainment during pouring. A free surface area of 110 m^2 for 1 ton of steel can be achieved, for example, by visualizing the metal stream during pouring to consist of droplets with a diameter of about 0.7 cm or of a cylindrical jet with a diameter of about 0.5 cm. Considering the large uncertainties in the exposure time and boundary layer thickness estimates, these values are not completely unrealistic.

Figure 21(b) shows that, in the present example of unprotected tapping and ladle filling (*i.e.,* for $(\bar{A}_s t_e) = 110$ m^{2}s), approximately 2.75 kg of solid inclusions and 0.55 m^3 of CO gas are produced. Also, 5.5 m^3 of air at standard conditions are needed to supply the oxygen. Since 1 ton of steel has a volume of only 0.13 m^3, this corresponds to an air-to-steel volume ratio of about 42. It can be expected that the preceding values represent an upper bound for unprotected

Table VI. Predicted Inclusion Properties and Ratios for Low- and High-Alloy Steels

(ΔC^O = 0.9 wt pct)	Low-Alloy Steel		CF8M Steel
	With CO Gas	Without CO Gas	
Average inclusion density (g/cm^3)	1.31×10^{-3}	3.23	3.08
Average inclusion molecular weight (g/mol)	93	149	83
Inclusion mass per mass of oxygen (O) consumed	2.27	1.95	2.30
Inclusion moles per mole oxygen (O_2) consumed	0.78	0.42	0.89

pouring of steel from a ladle into a mold in typical steel casting operations.

For completeness, several important reoxidation inclusion properties (average density and average molecular weight) and ratios (inclusion mass or moles per mass or moles of oxygen consumed) are summarized in Table VI. Values are included for both low- and high-alloy steels. The table also shows the large effect of the CO gas on the inclusion density for low-alloy steel.

VII. CONCLUSIONS

The model developed in this study predicts the composition of reoxidation inclusions in steel castings that form due to liquid steel being exposed to air during pouring from the ladle into the mold. It is shown how the inclusion composition varies with the mass of absorbed oxygen (ΔC^O). For a mass percentage of 0.9 wt pct oxygen, the predicted and previously measured inclusion compositions were found to agree for all steel grades investigated. The parametric studies allow for numerous interesting conclusions regarding the effect of steel grade and composition on the inclusion composition. The present model for the oxygen absorption rate shows under what conditions the 0.9 wt pct oxygen content can be achieved. One possibility is that the liquid metal stream during pouring is highly fragmented and consists of small droplets in which the oxygen content is uniform. If the liquid metal stream during pouring is more compact, on the other hand, the oxygen content of 0.9 wt pct can only be achieved in a relatively thin oxidation layer adjacent to the free surface. For unprotected liquid steel transfer operations, such as tapping and ladle filling, very large free surface areas are estimated based on the knowledge of the mass of the consumed alloy elements. The present findings point to the need for a more sophisticated reoxidation inclusion formation model. Such a model would need to account for the transport and reactions of the various chemical species inside the steel on a submillimeter scale. In addition, it would need to accurately predict the free surface area during pouring and the rates of oxygen transport through the air as a function of the flow conditions.

ACKNOWLEDGMENTS

This work was prepared with the support of the United States Department of Energy (DOE), Award No. DE-FC36-02ID14225. However, any opinions, findings, conclusions, or recommendations expressed herein are those of the authors and do not necessarily reflect the views of the DOE. We thank Malcolm Blair and Raymond Monroe of the SFSA for their helpful suggestions and guidance in this work. This article is based on a paper first presented at the 59th Technical and Operating Conference of the Steel Founders' Society of America (SFSA), Chicago, IL, Nov. 2005.

REFERENCES

1. J.M. Svoboda, R.W. Monroe, C.E. Bates, and J. Griffin: *AFS Trans.*, 1987, vol. 95, pp. 187-202.
2. J.A. Griffin and C.E. Bates: SFSA Research Report No. 104, SFSA, Crystal Lake, IL, Jan. 1991.
3. I.D. Sommerville and E.J. McKeogh: *Continuous Casting of Steel: Proc. 2nd Process Technology Conf.*, Chicago Meeting, ISS-AIME, Warrendale, PA, 1981, pp. 256-68.
4. K.D. Carlson and C. Beckermann: *Proc. 58th Technical and Operating Conf.*, SFSA, Crystal Lake, IL, 2004.
5. V. Brabie, M. Kawakami, and S. Eketorp: *Scand. J. Metall.*, 1975, vol. 4, pp. 273-83.
6. V. Brabie: *Scand. J. Metall.*, 1976, vol. 5, pp. 185-92.
7. K.W. Lange and P. Massard: *Arch. Eisenhuettenwes.*, 1977, vol. 48 (8), pp. 415-20.
8. A.F. Vishkarev and L.S. Gorokhov: *Steel USSR*, 1991, vol. 21, pp. 196-98.
9. H. Sun and R.D. Pehlke: *Metall. Mater. Trans. B*, 1995, vol. 26B, pp. 335-44.
10. H. Sun and R.D. Pehlke: *Metall. Mater. Trans. B*, 1996, vol. 27B, pp. 854-64.
11. K. Sasai and Y. Mizukami: *Iron Steel Inst. Jpn. Int.*, 1996, vol. 36 (4), pp. 388-94.
12. K. Sasai and Y. Mizukami: *Iron Steel Inst. Jpn. Int.*, 1998, vol. 38 (4), pp. 332-38.
13. K. Sasai and Y. Mizukami: *Iron Steel Inst. Jpn. Int.*, 2000, vol. 40 (4), pp. 40-47.
14. H. Goto and K. Miyazawa: *Iron Steel Inst. Jpn. Int.*, 1998, vol. 38 (3), pp. 256-59.
15. K.C. Hsieh, S.S. Babu, J.M. Vitek, and S.A. David: *Mater. Sci. Eng., A*, 1996, vol. 215, pp. 84-91.
16. B. Sundman: *Thermo-Calc User's Guide, Version P*, Royal Institute of Technology, Stockholm, 2002.
17. C. Eijk, Ø. Grong, and J. Walmsley: *Mater. Sci. Technol.*, 2000, vol. 16, pp. 55-64.
18. W.S. Lyman and F.W. Boulger: SFSA Research Report No. 48, SFSA, Crystal Lake, IL, Feb. 1961.
19. J.A. Griffin and C.E. Bates: SFSA Research Report No. SoRI-EAS-86-682, SFSA, Crystal Lake, IL, 1986.
20. J.A. Griffin and C.E. Bates: SFSA Research Report No. SoRI-EAS-86-810, SFSA, Crystal Lake, IL, 1986.
21. R.B. Bird, W.E. Stewart, and E.N. Lightfoot: *Transport Phenomena*, John Wiley & Sons, Inc., New York, NY, 1960, p. 512.
22. W.E. Ranz and W.R. Marshall: *Chem. Eng. Progr.*, 1952, vol. 48, pp. 141–46.
23. F. Kreith and D.Y. Goswami: *The CRC Handbook of Mechanical Engineering*, 2nd ed., CRC Press LLC, Boca Raton, FL, 2004, p. A-2.
24. T.E. Brower, J.W. Bain, and B.M. Larsen: *Trans. AIME*, 1950, vol. 188, pp. 851-61.